

Submesoscale Dynamics of a Gulf Stream Frontal Eddy in the South Atlantic Bight

JONATHAN GULA

Laboratoire de Physique des Océans, Université de Bretagne Occidentale, Brest, France

M. JEROEN MOLEMAKER AND JAMES C. MCWILLIAMS

Department of Atmospheric and Oceanic Sciences, University of California, Los Angeles, Los Angeles, California

(Manuscript received 21 December 2014, in final form 9 November 2016)

ABSTRACT

Frontal eddies are commonly observed and understood as the product of an instability of the Gulf Stream along the southeastern U.S. seaboard. Here, the authors study the dynamics of a simulated Gulf Stream frontal eddy in the South Atlantic Bight, including its structure, propagation, and emergent submesoscale interior and neighboring substructure, at very high resolution ($dx = 150$ m). A rich submesoscale structure is revealed inside the frontal eddy. Meander-induced frontogenesis sharpens the gradients and forms very sharp fronts between the eddy and the adjacent Gulf Stream. The strong straining increases the velocity shear and suppresses the development of barotropic instability on the upstream face of the meander trough. Barotropic instability of the sheared flow develops from small-amplitude perturbations when the straining weakens at the trough. Small-scale meandering perturbations evolve into rolled-up submesoscale vortices that are advected back into the interior of the frontal eddy. The deep fronts mix the tracer properties and enhance vertical exchanges of tracers between the mixed layer and the interior, as diagnosed by virtual Lagrangian particles. The frontal eddy also locally creates a strong southward flow against the shelf leading to topographic generation of submesoscale centrifugal instability and mixing. In eddy-resolving models that do not resolve these submesoscale processes, there is a significant weakening of the intensity of the upwelling in the core of the frontal eddies, and their decay is generally too fast.

1. Introduction

Meanders and eddies are ubiquitous in the Gulf Stream along the U.S. seaboard in the South Atlantic Bight (SAB), between the Florida Strait and Cape Hatteras (Fig. 1). Large meanders are visible most of the time on the inshore side of the Gulf Stream, with cyclonic frontal eddies propagating along the shelf. These frontal eddies occur where the Gulf Stream interacts with the slope and shelf. They are formed in the troughs of northward-propagating meanders and consist of deeply upwelled cold domes. They have typical wavelengths of 100–250 km and propagate downstream at speeds of 30–70 km day⁻¹ every 2–14 days (e.g., Glenn and Ebbesmeyer 1994, and references therein). Typical cross-stream length scales for frontal eddies are 30–50 km

upstream of the Charleston Bump (south of 31°N; Fig. 1) and can reach up to 100 km downstream. They are often associated with shallow warm filaments, known as “shingles” (von Arx et al. 1955), which form at the surface and extend from the leading meander crest along the shoreward side of the cold dome.

A typical example of satellite-observed sea surface temperature (SST) of the Gulf Stream along the SAB is shown in Fig. 1 during early spring (15 March 2013). Meanders and perturbations are seen all along the shoreward front of the Gulf Stream. Large frontal eddies are seen downstream of the Charleston Bump. The large frontal eddy visible at 32.5°N, 77.5°W has additional smaller-scale perturbations on its rim.

a. Overview of eddy variability along the SAB

The Charleston Bump, a deep-water topographic feature, has been identified as a preferred region for eddy generation using satellite-based measurements and statistics. Satellite observations show a steady increase of the variance of the stream position between

Corresponding author address: Jonathan Gula, Laboratoire de Physique des Océans, Université de Bretagne Occidentale, 6 Avenue Le Gorgeu, CS 93837, 29238 Brest, France.
E-mail: jonathan.gula@univ-brest.fr

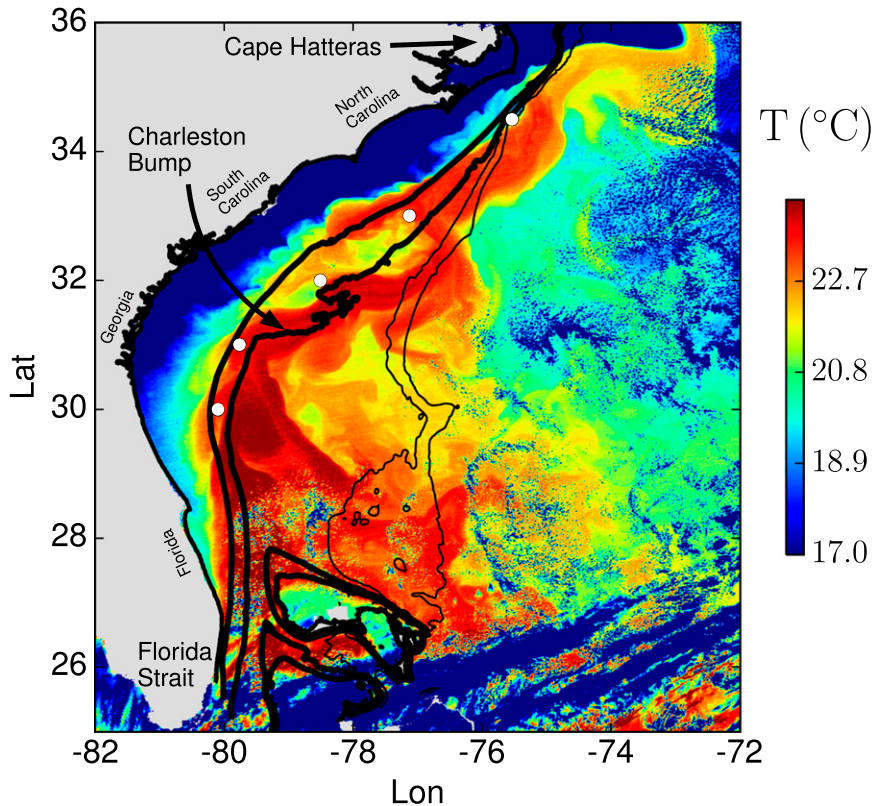


FIG. 1. Observed SST of the Gulf Stream on 15 Mar 2013. Data from MODIS-*Aqua*. Black contours indicate the 200-, 600-, 1000-, and 2000-m isobaths. The warm Gulf Stream is deflected eastward at the Charleston Bump location. Large meanders form downstream of the bump with frontal eddies in between detraining water from the leading wave crest of the meander. The large frontal eddy visible at 32.5°N, 77.5°W has additional smaller-scale perturbations on its rim. The white dots indicate the locations chosen for pointwise time series of SSH.

the Florida Strait and the bump, followed by a sharp increase downstream of the bump and a gradual decay from approximately 33°N to Cape Hatteras (Olson et al. 1983). Energy is transferred from the mean flow to the eddies following the Florida Strait and the Charleston Bump, with regions of eddy to mean conversion in between (Dewar and Bane 1985; Lee et al. 1991). The effect of the topography on the instability of the flow and the development and evolution of meanders and eddies is studied in Gula et al. (2015a,b) using realistic high-resolution simulations. Barotropic conversion from mean to eddy kinetic energy through horizontal Reynolds stress and baroclinic conversion from eddy potential to eddy kinetic energy through vertical eddy fluxes of buoyancy both contribute to the along-stream variations of eddy kinetic energy. The eddy activity between the strait and the bump is mostly a barotropic mechanism driven by current-topography interactions. The positive relative vorticity on the cyclonic side of the Gulf Stream is strongly intensified in the Florida Strait due to topographic drag along the continental slope.

Downstream from the strait the current partially separates, becomes unstable to horizontal shear instability, rolls up, and forms streets of submesoscale vortices (Gula et al. 2015b). The baroclinic instability is stabilized by the cross-stream slope everywhere except past the Charleston Bump where the Gulf Stream moves seaward and the topographic constraint is locally weakened. At the location of the Charleston Bump the flow is locally strongly unstable through a mixed barotropic–baroclinic instability process and regularly forms large mesoscale frontal eddies (Gula et al. 2015a). As a result, the amplitudes of the meanders rapidly increase as they progress northeastward. The continental slope steepens and stabilizes baroclinic instability downstream of the Charleston Bump. Eddy kinetic energy is converted back into mean kinetic energy, a process that results in decreasing eddies and meander amplitudes.

b. Observations of frontal eddies

Frontal eddies between Georgia and North Carolina have been observed in numerous studies over the

TABLE 1. Summary of observations of northward propagating meanders and eddies.

	Phase speed (km day ⁻¹)	No. of Eddies	Location	Observation period	Source
Le75	34	1	29°–31°N	March 1975	Legeckis (1975)
VCBK79	30 ± 15	>10	28°–30.5°N	1973–1977	Vukovich et al. (1979)
VC80	24 ± 10	>100	32°–34°N	January–May 1977	Vukovich and Crissman (1980)
BBL81	32	1	33°–34°N	February 1979	Bane et al. (1981)
	35	1	33°–34°N	February 1979	Bane et al. (1981)
BB81	30	>10	33°–34°N	January–May 1979	Brooks and Bane (1981)
	48	>10	33°–34°N	January–May 1979	Brooks and Bane (1981)
LAL81	36	1	31°–32°N	April 1977	Lee et al. (1981)
	40	1	31°–32°N	April 1977	Lee et al. (1981)
BB83	40	>10	33°–34°N	1979	Brooks and Bane (1983)
LA83	43–60	>10	29°–32°N	February–June 1980	Lee and Atkinson (1983)
MCPY84	28	1	31°–32°N	April 1980	McClain et al. (1984)
	47	1	28.5°–30°N	April 1980	McClain et al. (1984)
GE94	50	1	34.5°N	May 1987	Glenn and Ebbesmeyer (1994)

past 40 yr. Lee and Atkinson (1983) used long-term measurements to study the low-frequency current and temperature variability upstream of the bump between 30° and 32°N and found that it is dominated by cyclonic frontal eddies with an occurrence once every 5–9 days and propagating northward at speeds between 40 and 60 km day⁻¹ with an along-shelf coherence of about 100 km. McClain et al. (1984) observed two frontal eddies offshore of Georgia propagating at 28 and 47 km day⁻¹ with increasing speeds as they approached the bump. Measurements by Lee et al. (1981) along the Georgia shelf found that eddies propagate at average speeds of 35 km day⁻¹ with one eddy every 2 weeks. Downstream of the Charleston Bump, eddies with alongshore diameters of 150 km and cross-shore diameters of 50 km were observed to propagate downstream at 24 km day⁻¹ with a recurrence interval of 6 days by Vukovich and Crissman (1980). Bane et al. (1981) and Brooks and Bane (1981) found propagation speeds between 30 and 35 km day⁻¹ for several eddies off Onslow Bay. Eddies with propagation speeds up to 40 km day⁻¹ were also observed by Brooks and Bane (1983) off North Carolina. Glenn and Ebbesmeyer (1994) described extensively the structure and propagation of one Gulf Stream frontal eddy observed along the North Carolina shelf break. The cross-stream and along-stream dimensions of the eddy are approximately 20 and 40 km, respectively. Its propagation speed increased in the vicinity of Cape Hatteras from 50 km day⁻¹ at 34.4°N to 62 km day⁻¹ at 35.5°N. Year-long measurements upstream of Cape Hatteras by Savidge and Bane (2004) revealed meanders with periodicity of 3 to 8 days and 180 to 380 km in wavelength that propagate downstream along the Gulf Stream at speeds between 40 to 55 km day⁻¹. A summary of the observed phase speeds of the meanders

and eddies from various sources is provided in Table 1.

c. Impact on cross-shelf transport and biological productivity

The frontal eddies have strong implications for the biological production in the South Atlantic Bight (Lee et al. 1991). The cold core of the frontal eddies is a result of upwelling of cold and freshwater from the Gulf Stream thermocline (Lee et al. 1981). Lee and Atkinson (1983) measured upwelling at a mean rate of approximately 10 m day⁻¹ within the cold dome of frontal eddies. The upwelling in the core of the frontal eddies pumps nutrient-rich bottom waters toward the surface, resulting in high levels of ocean productivity. Elevated phytoplankton pigment concentrations are observed within eddies (Yoder et al. 1981; McClain and Atkinson 1985), and specific seabird species are shown to be more abundant above the upwelled cold core of these eddies (Haney 1986). Eddies dominate cross-shelf exchange processes with the adjacent shelf water, which have important dynamical, ecological, and water quality implications (Blanton et al. 1981; Lee and Atkinson 1983; McClain et al. 1984; Yoder et al. 1985; Lee et al. 1991). The biological production on the outer to middle continental shelf is controlled by frontal eddies; there are year-round phytoplankton blooms on the outer shelf in the upwelled cold water and blooms in the subsurface intrusions upwelled onto the middle shelf from May to October (Yoder et al. 1985). The frontal eddies also shape the distribution of larval fish by mixing larvae from the outer continental shelf and the Gulf Stream and entraining them into the eddy circulation at the margins as wraparound filaments (Govoni et al. 2013).

In the present study, we investigate the dynamics of the frontal eddies along the seaboard with a set of

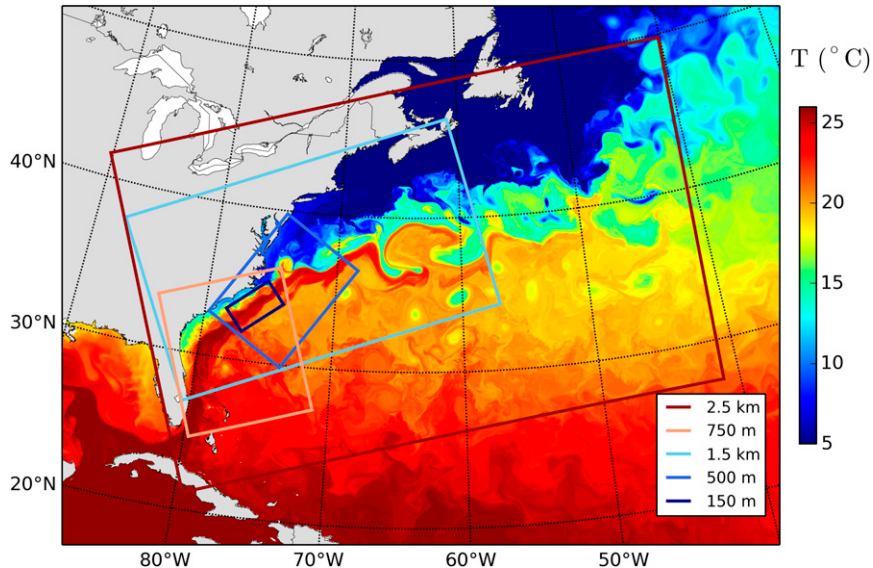


FIG. 2. SST in the region of the Gulf Stream at the end of winter as simulated by ROMS. The parent domain ($\Delta x \approx 6$ km) covers most of the Atlantic Ocean. There are two distinct sequences of child grids with $\Delta x \approx 2.5$ km and 750 m and $\Delta x \approx 1.5$ km, 500 m, and 150 m, respectively. The boundaries of the successive nested domains are delineated by colored lines.

realistic, very high-resolution simulations. The paper is organized as follows: The simulation setup is presented in section 2. Characteristics of the frontal eddies and their amplification mechanisms at the Charleston Bump are described in section 3. The structure and propagation of a frontal eddy are studied in section 4. In section 5, the emergent submesoscale interior and neighboring substructure of the frontal eddy are analyzed in more detail. We explore the dynamics of the submesoscale processes and investigate their impacts for the mixing and vertical exchange of tracers between the interior and the surface. Conclusions are presented and discussed in section 6.

2. Simulation setup

The high-resolution realistic simulations of the Gulf Stream are performed with the Regional Oceanic Modeling System (ROMS; Shchepetkin and McWilliams 2005). We use a nesting approach with successive horizontal grid nesting refinements from a parent grid resolution of $\Delta x \approx 6$ km, covering most of the Atlantic Ocean, to two distinct sequences of child grids with $\Delta x \approx 2.5$ km and 750 m (Gula et al. 2015a) and $\Delta x \approx 1.5$ km, 500 m, and 150 m (Gula et al. 2014). These successive domains are all shown in Fig. 2. Vertical mixing of tracers and momentum is done with a K-profile parameterization (KPP; Large et al. 1994). The effect of bottom friction is parameterized

through a logarithmic law of the wall with a roughness length $Z_0 = 0.01$ m. Lateral oceanic forcings for the largest domain, as well as surface forcings for all simulations, are climatological. Boundary data for the largest domain covering the Atlantic Ocean are taken from the monthly averaged SODA ocean climatology (Carton and Giese 2008). Simulations are all forced at the surface by high-frequency winds constructed from a climatology of QuikSCAT scatterometer winds [Scatterometer Climatology of Ocean Wind (SCOW); Risien and Chelton 2008] with the addition of daily winds that have the right amount of climatological variance. Heat and freshwater atmospheric forcing are from COADS (Silva et al. 1994). More technical details on the configuration may be found in Gula et al. (2015a).

Statistics on the characteristics of the meanders and eddies along the SAB described in section 3 are computed using outputs from 1 yr of simulation for the domain covering the SAB with horizontal resolution $\Delta x = 750$ m (Fig. 2). All the numerical results described in sections 4 and 5 come from the highest level of grid refinement that yields 4 months of simulation for a domain that covers the Gulf Stream upstream of Cape Hatteras with horizontal resolution $\Delta x = 150$ m and 1330×2400 grid points (Fig. 2). This simulation follows, in particular, the evolution of a typical example of a frontal eddy propagating along the shelf during wintertime. Such resolution allows us to resolve the detail of the

submesoscale dynamics of the different structures in the vicinity of the frontal eddy.

3. Frontal eddies along the seaboard

We describe in this section the formation and propagation of the mesoscale frontal eddies that are routinely observed between the bump and Cape Hatteras in the simulations and compare their characteristics to observations. These eddies have phase speeds, dimensions, and shapes that change while they propagate along the shelf and in particular in the vicinity of the Charleston Bump.

The spatial distribution of sea surface height (SSH) variability in the simulation is compared to altimetric observations in Gula et al. (2015a, their Fig. 11). The model and altimetric data display similar scales and patterns of enhanced variability, identically strong in a rather narrow band along the Gulf Stream path north of 31.5°N over and to the northeast of the bump, with a maximum at 32°N.

To get a statistical view of the meanders and eddies phase speeds, we compute cross correlations between time series of SSH at different locations along the Gulf Stream path between 30°N and 34.5°N for model results and for altimetric observations. The altimetric observations are the 2000–12 AVISO daily sea level anomalies (www.aviso.altimetry.fr) mapped on a $\frac{1}{4}^\circ \times \frac{1}{4}^\circ$ Cartesian grid. Cross correlations are a measure of the similarity of the two time series as a function of time-lag applied to one of them. Correlation coefficients are plotted in Fig. 3 as a function of velocity, corresponding to the distance between the two locations divided by the time-lag used to compute the correlation between the signals at the two locations. These velocity values represent the propagation speed of an equivalent propagating feature that would explain the correlation between the signals at the two locations (assuming a constant propagation speed between them) for each value of the time-lag. These velocity values can be compared directly to the propagation speed of the eddies observed in the different sectors of the SAB (Table 1). Phase speed values extracted from the observational studies compiled in Table 1 have been plotted on top of Fig. 3 in the corresponding SAB sector using circles for individual measurements and segments for long-term measurements.

There are significant positive cross correlations between the SSH variations at the different locations in both the model and the observations, which are associated with meanders and eddies that propagate between 10 and 60 km day $^{-1}$. These characteristics vary

somewhat along the Gulf Stream. The velocity corresponding to the maximum correlation shifts toward larger values between 30° and 32°N, where it reaches 40 km day $^{-1}$. This is consistent with an acceleration of the eddies upstream of the bump (McClain et al. 1984). The velocity corresponding to the maximum correlation diminishes between 32° and 33°N, down to about 25 km day $^{-1}$ due to the influence of the bump, matching the characteristics of the larger eddies observed in this region (Vukovich and Crissman 1980). It increases again steadily between the bump and Cape Hatteras. The maximum correlations are seen for propagation speeds between 30 and 50 km day $^{-1}$, corresponding to the characteristics of the observed frontal eddies in this region (Bane et al. 1981; Brooks and Bane 1981, 1983; Glenn and Ebbesmeyer 1994).

There is not necessarily continuity between the smaller frontal eddies upstream of the bump and the large slope eddies downstream of the bump, but they have similar kinematic properties (Brooks and Bane 1981; Bane et al. 1981). Individual events of frontal eddies propagating through the bump region and undergoing amplification have been observed and documented (Legeckis 1979; Lee et al. 1981), and one typical example from the simulation is shown Fig. 4 using SSH anomaly time series at different locations along the Gulf Stream path. Cyclonic features are characterized by negative SSH anomalies. A small negative SSH anomaly, visible at 29°N on 24 February, shows such a cyclonic feature propagating along the shelf, slowly growing and deepening on its way to the bump. Between 31° and 32.5°N, at the location of the Bump, it is strongly amplified and turns into a large cyclonic frontal eddy. The frontal eddy later slowly weakens on its way to Cape Hatteras. Another similar frontal eddy is seen forming about two weeks later, which is a typical recurrence interval for these eddies.

The Gulf Stream is locally unstable when the flow is deflected seaward at the bump (Gula et al. 2015a). Topographic variations in the along-stream direction along the SAB correspond to a stabilizing bottom slope except for a gap with a limited extent where the flow is baroclinically unstable. The stability of a buoyant coastal current over such a bathymetric gap has also been studied by Bracco and Pedlosky (2003) numerically in a two-layer quasigeostrophic (QG) model and by Wolfe and Cenedese (2006) in laboratory experiments. Both concluded that the instability was purely local and neither influenced by the stability of the flow outside of the gap nor by the abruptness of the transition at the edges of the gap. They found that for gap lengths on the order of several Rossby deformation radii, as is the case here, the nonlinear equilibration of the local instability

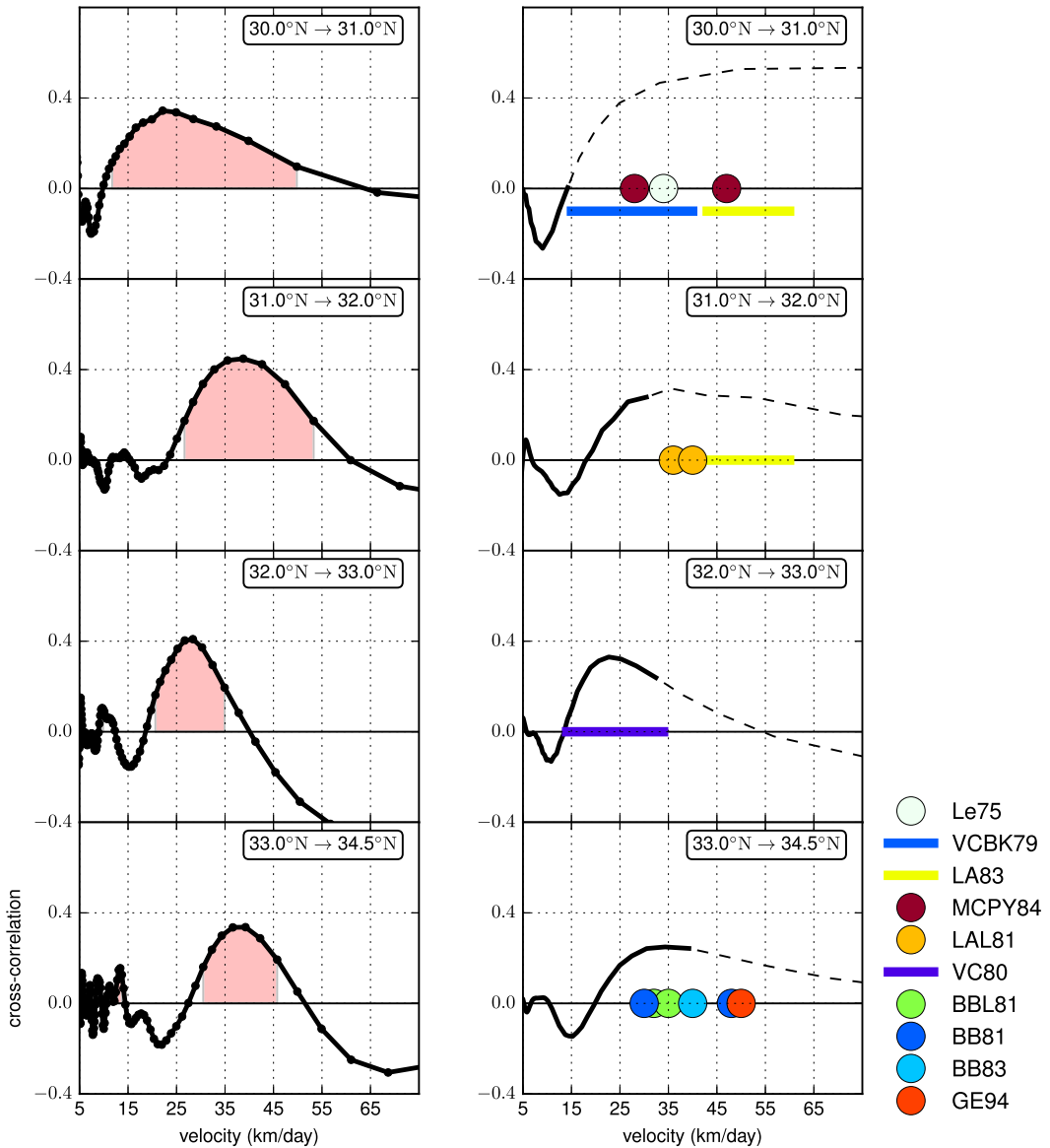


FIG. 3. Cross correlations between pointwise time series of SSH at different locations along the Gulf Stream path (marked as white dots in Fig. 1) for (left) 1 yr of ROMS simulation and (right) 12 yr of satellite observations from AVISO. The correlation coefficients are plotted as a function of a velocity, corresponding to the distance between the two points divided by the time-lag used to compute the cross correlation. Filled red areas on the left panels indicate regions where correlations are positive and p values are lower than 0.01. Colored circles and segments on the right panels indicate the phase speeds values extracted from the observational studies compiled in Table 1. Cross correlations for observed SSH from AVISO may be altered by the temporal interpolation applied to the satellite measurements to produce daily data and are plotted as a dashed line when the time-lag is lower than 7 days.

process would form coherent vortices that could escape the gap and propagate downstream.

The formation of such large frontal eddy over the bump is shown in Fig. 5 using maps of vorticity, temperature, and vertical velocity. A small meander visible initially at 31°N , 79.5°W has been formed upstream of the bump. The positive vorticity is attached to an upwelled dome of cold water. The propagating meander has a

characteristic positive-negative signature on the vertical velocity field, with upwelling on the leading edge of the cold dome and downwelling on the trailing edge (Osgood et al. 1987). There is cyclonic intensification through vortex stretching as the meander crosses the nose of the bump. The topography is acting to reinforce the positive vorticity and to increase the upwelling in the center of the meander. The flow can then form a quasi-blocked state as

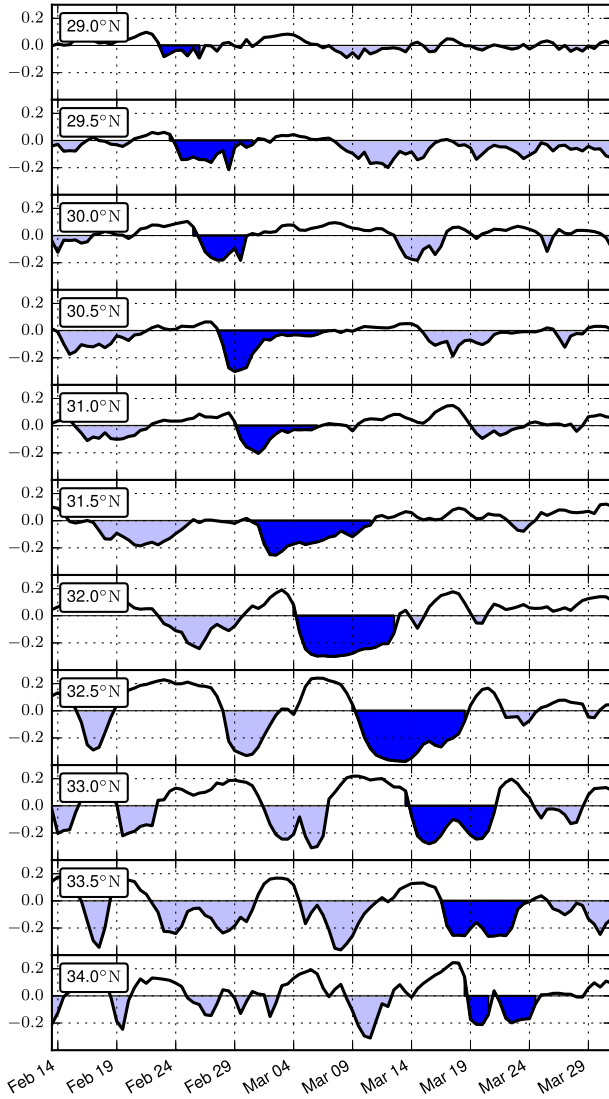


FIG. 4. Time series of SSH anomaly at different locations along the Gulf Stream path for 50 days. Negative anomalies characterizing cyclonic features are filled with blue. The dark blue negative anomaly follows the propagation of one typical frontal eddy.

the meander considerably slows down. While in such a blocked state, the high positive vorticity on the cyclonic side of the Gulf Stream gets advected into the center of the meander and strengthens its cyclonic circulation. At the time of Fig. 5j, the slope eddy reaches its maximum size, about 160 km in the along-stream direction and 80 km in the cross-stream direction, and is slowly advected downstream.

4. Structure and evolution of a frontal eddy

We investigate in this section the dynamics of a frontal eddy while it propagates along the shelf between the

Charleston Bump and Cape Hatteras. It has been previously described how frontal eddies are amplified or generated at the bump, and we focus now on the propagation and evolution of a frontal eddy. We follow a particular example with characteristics typical of large frontal eddies that form downstream of the bump.

A sequence of SST snapshots at 3-day intervals showing the evolution and propagation of the frontal eddy is plotted in Fig. 6. The frontal eddy is initially located at 33°N, 77°W in Fig. 6a and propagates downstream with a velocity about 25 km day^{-1} . The frontal eddy cross- and alongshore scales are 50 and 100 km, respectively, at the time of Fig. 6a. The characteristics of the frontal eddy are identical to those of the eddies observed by Vukovich and Crissman (1980) and match the description of the large-amplitude meanders designated as biweekly meanders by Bane and Dewar (1988).

We clearly see the cold upwelled water in the meander trough, and the shallow warm filament (shingle) detached from the wave crest at the surface along the shoreward side of the cold dome, as described in Lee et al. (1991). The offshore side of the frontal eddy follows the 600-m isobath. While the eddy converges toward Cape Hatteras, its size diminishes and its propagation speed increases. It is squeezed against the topographic contours and ultimately is sheared apart as the slope becomes steeper and deeper in the vicinity of Cape Hatteras.

Vertical sections of temperature and velocity anomalies are shown at locations following the propagation of the eddy along the shelf in Fig. 7. The frontal eddy is initially entirely on the slope, and the cyclonic circulation of the frontal eddy extends throughout the water column (Figs. 7a,e). It leaves the continental slope progressively as the slope steepens and becomes almost vertical before reaching Cape Hatteras (Figs. 7d,h).

This is in agreement with observed characteristics of frontal eddies that are on average larger, more intense, and move more slowly immediately downstream of the Charleston Bump than in regions farther downstream where the slope is steeper (Vukovich and Crissman 1980). The decay of the eddies is consistent with the eddy-to-mean energy conversion in this region (Gula et al. 2015a), resulting in decreasing meander and eddy amplitudes and in reinforcing the mean flow.

5. Submesoscale structures in a frontal eddy

A very rich submesoscale structure is revealed around and inside the frontal eddies in the high-resolution simulations. Small-scale perturbations can be spotted around the rim of the simulated frontal eddy (Fig. 6b). Submesoscale features are also visible in the observed

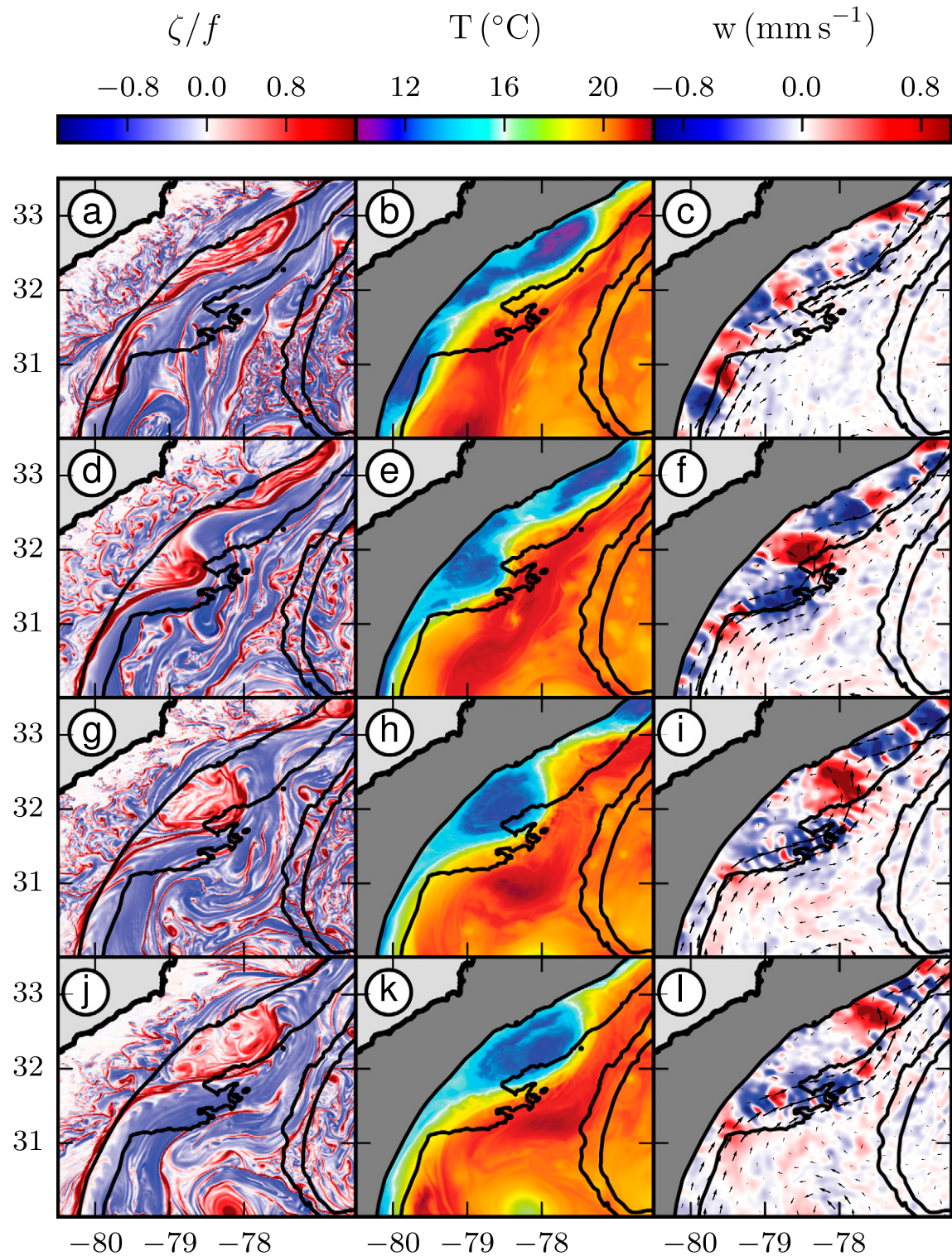


FIG. 5. The formation of a large frontal eddy in snapshots of (left) surface relative vorticity normalized by f , (center) temperature at $z = -200 \text{ m}$, and (right) vertical velocity at $z = -200 \text{ m}$. The time interval between consecutive rows is 3.5 days. Topography is shown in black contours for the levels $-200, -600, -1000$, and -2000 m .

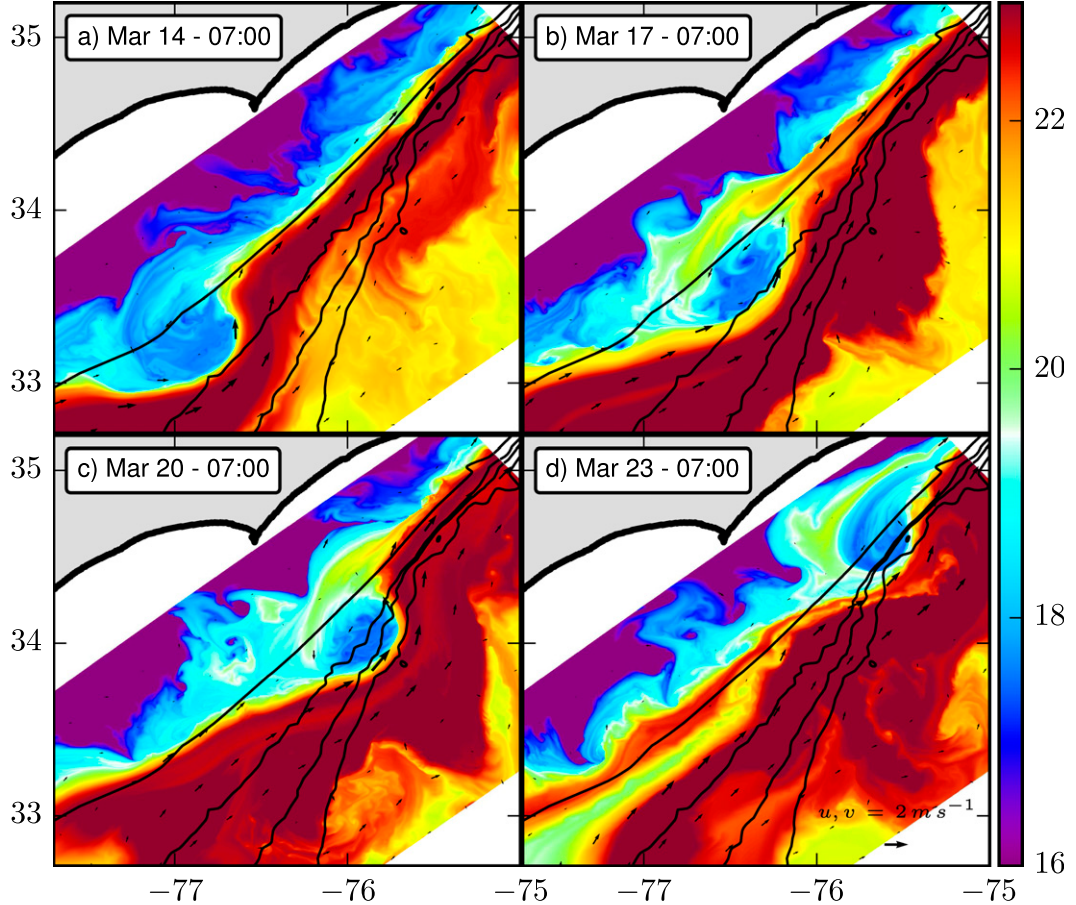


FIG. 6. Simulated SST every 3 days downstream from the Charleston Bump and south of the Gulf Stream separation point. A large frontal eddy, visible as a cold anomaly, propagates with a velocity about $20\text{--}30 \text{ km day}^{-1}$. Surface velocities are the black vectors. Topography is shown in black contours for the levels -200 , -600 , -1000 , and -2000 m .

satellite SST in Fig. 1, around the frontal eddy located at 32.5°N , 77.5°W that has very similar characteristics to the frontal eddy described here.

To illustrate the changes associated with the increase in the model horizontal resolution, horizontal sections of salinity at the surface and at $z = -100 \text{ m}$ (below the mixed layer) are shown in Fig. 8 for the frontal eddy of Fig. 6 for three successive grid nests with horizontal resolutions of $\Delta x \approx 1.5 \text{ km}$ ($\delta_{1.5\text{km}}$), $\Delta x \approx 500 \text{ m}$ ($\delta_{500\text{m}}$), and $\Delta x \approx 150 \text{ m}$ ($\delta_{150\text{m}}$). There are, as expected, increasingly sharper gradients when going from $\delta_{1.5\text{km}}$ to $\delta_{150\text{m}}$ due to the higher resolution and the weaker model diffusion. The negative salinity anomaly increases in the core of the eddy at depth in $\delta_{500\text{m}}$ and $\delta_{150\text{m}}$, showing that the upwelling is intensified as the resolution is increased. The weakening of the frontal eddy while it propagates toward Cape Hatteras is amplified, and the propagation speed increases faster in the lower-resolution simulation $\delta_{1.5\text{km}}$. The salinity

minimum is also more pronounced in the surface layer in $\delta_{500\text{m}}$ and $\delta_{150\text{m}}$, showing the connection of the upwelled water to the surface. Additional smaller-scale salinity patterns are visible inside the frontal eddy core at the surface in $\delta_{150\text{m}}$ that are not present in $\delta_{1.5\text{km}}$ and only partially present in $\delta_{500\text{m}}$. These submesoscale patterns have horizontal scales of $5\text{--}10 \text{ km}$ and have strong minima in salinity.

A closer view of the inside structure of the frontal eddy in the highest-resolution nest is shown in Fig. 9. The low-salinity patches are associated with vortical structures with high relative vorticity values ($\zeta > 2f$, where f is the Coriolis frequency). A vertical section crossing through these structures is plotted in the bottom panel of Fig. 9. The low-salinity values are connected to the upwelled cold and freshwater from the frontal eddy core. The vortical structures appear to provide additional upwelling and enhance the exchange of interior cold core water with the surface.

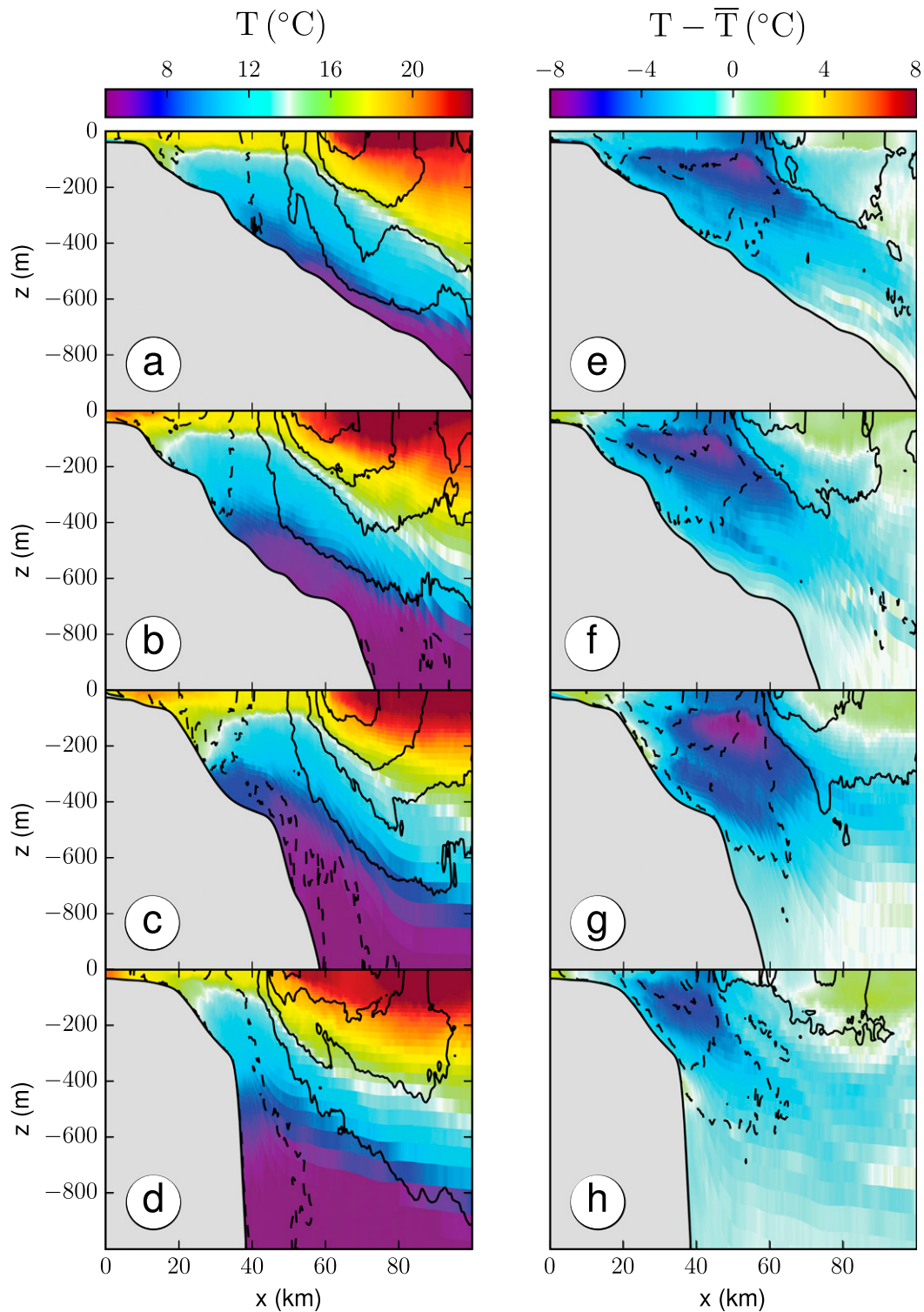


FIG. 7. Temperature (colors) and along-shelf velocity (black contours) in cross-shelf sections at the center of the frontal eddy (every 3 days) corresponding to the four panels of Fig. 6. (left) Total fields and (right) perturbations relative to the time-mean flow.

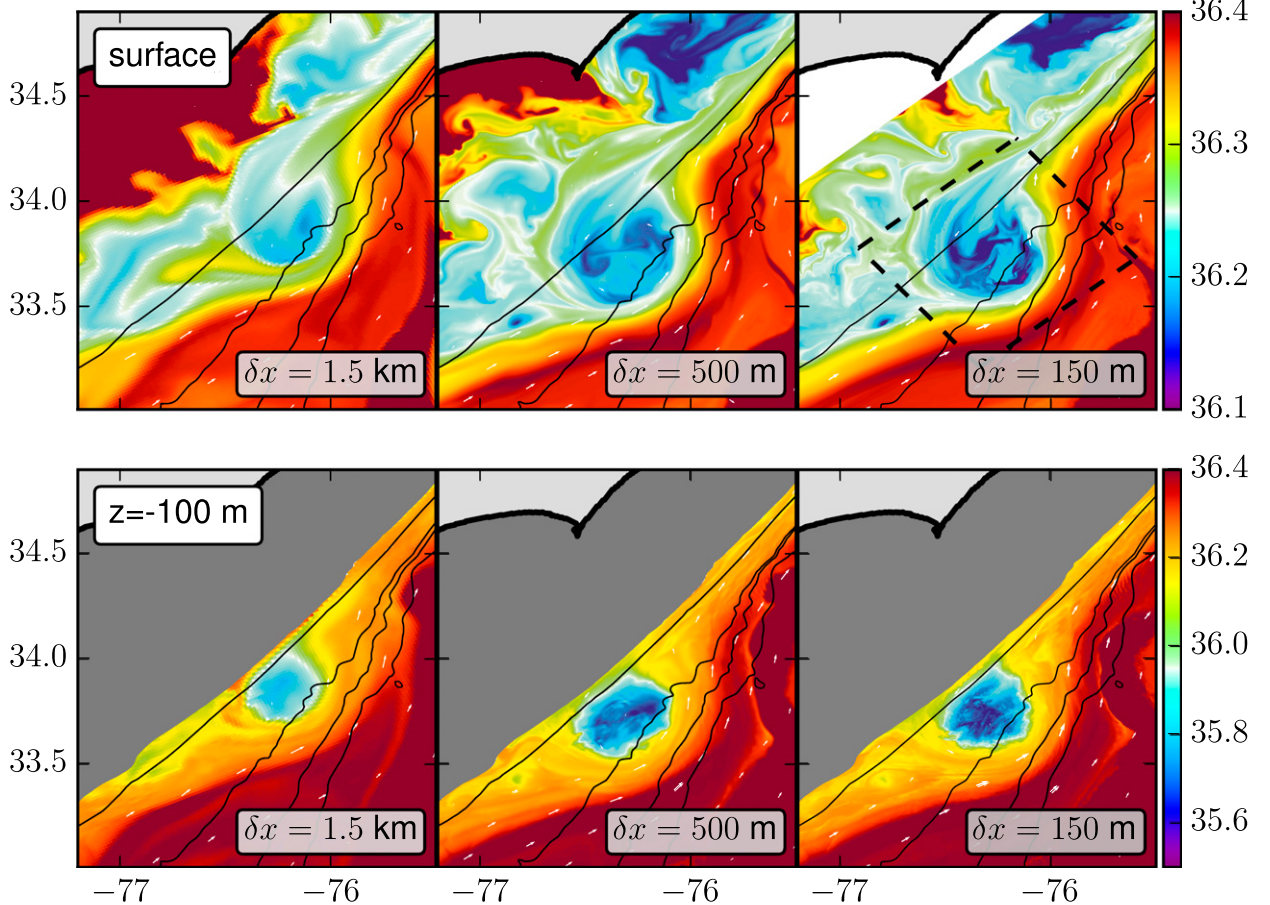


FIG. 8. Salinity (psu; colors) in the successive nests $\delta_{1.5\text{km}}$, $\delta_{500\text{m}}$, and $\delta_{150\text{m}}$ for the frontal eddy of Fig. 6 (on Mar 18) at (top) the surface and (bottom) $z = -100 \text{ m}$. Velocities are the white vectors. Topography is shown in black contours for levels -200 , -600 , -1000 , and -2000 m . The dashed black box shows the domain plotted in Figs. 9 and 10.

Maps of relative vorticity $\zeta = v_x - u_y$, with (u, v) as the (x, y) components of the horizontal flow, and the Okubo–Weiss parameter $\text{St}^2 - \zeta^2$, where $\text{St} = \sqrt{(u_x - v_y)^2 + (v_x + u_y)^2}$ is the strain rate, are shown in Figs. 10a and 10b. The submesoscale cyclonic vortical structures can be seen forming in the interior of the frontal eddy, as indicated by the positive vorticity and negative Okubo–Weiss parameter values. The strong strain rate (Fig. 10d) and positive Okubo–Weiss parameter values on the Gulf Stream interior edge of the eddy indicate a submesoscale strain-induced frontogenesis acting on the sharp front of the Gulf Stream, which is confirmed in the frontal sharpness and frontogenetic tendency discussed in section 5a.

a. Frontogenesis around the frontal eddy

The horizontal buoyancy gradients are very strong at the rim of the eddy on the offshore, Gulf Stream side, especially in the trough of the meander (Fig. 10c). This sharp front between the frontal eddy and the

stream is instantaneously composed of multiple submesoscale fronts. They appear as elongated vorticity filaments on the stream interior edge of the eddy. The frontal region is very deep and reaches down to 200 m (Fig. 9).

The horizontal strain rate has a very strong signal on the upstream face of the trough and weakens on the downstream face (Fig. 10d). To distinguish the strain induced by the geostrophic flow from the strain induced by the ageostrophic secondary circulation acting on the fronts or filaments in response to this background straining, the total strain can be decomposed into components that are due to the divergent or nondivergent parts of the flow (Gula et al. 2014). This decomposition is shown in Fig. 3 of Gula et al. (2014) for the 1.5-km resolution nest upstream of Cape Hatteras where a similar frontal eddy is seen propagating along the shelf. It shows that the strain on the rim of the eddy is primarily a result of the horizontal mesoscale flow generated by the interaction of the frontal eddy and the

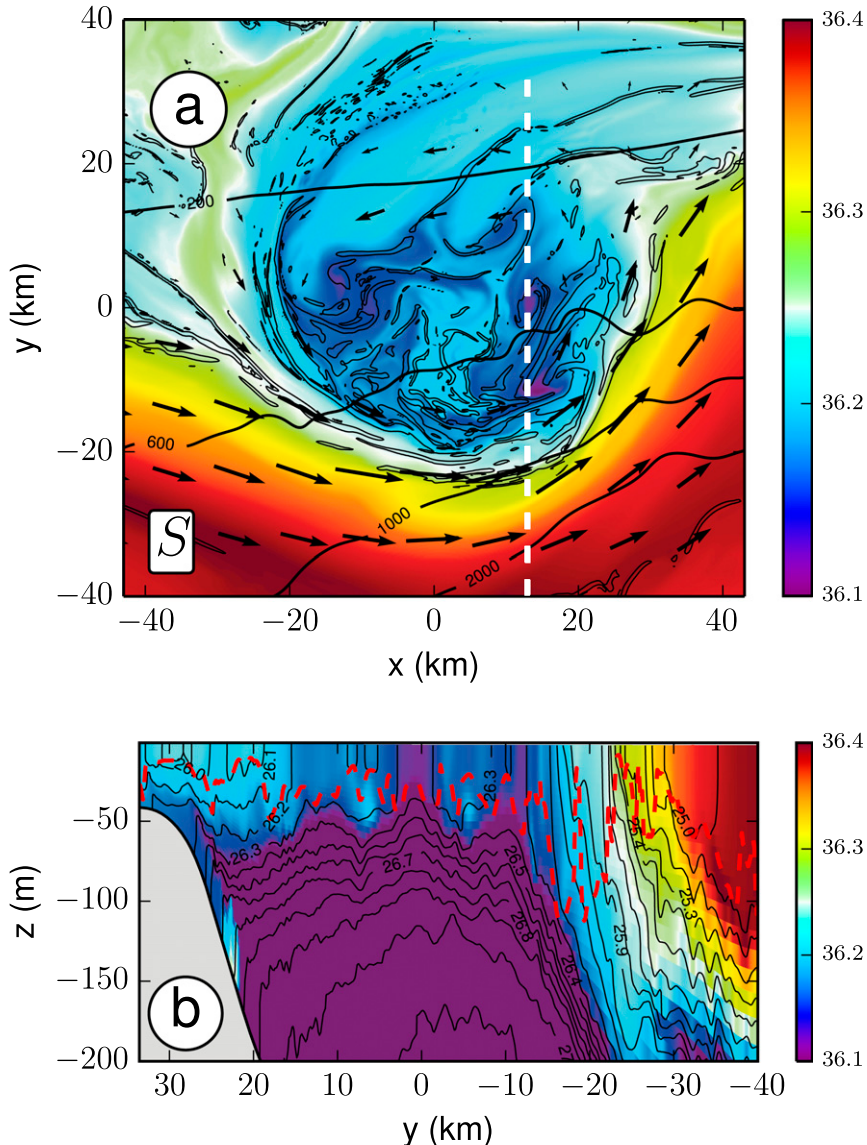


FIG. 9. (top) Salinity at $z = -10$ m (psu; colors) and relative vorticity (at $\pm 2f$ in black contours) for the frontal eddy of Fig. 8, showing the intrafrontal eddy submesoscale vortices. Topography is shown in thin black contours for levels -200 , -600 , -1000 , and -2000 m. (bottom) Vertical cross-shelf section of salinity along the white dashed line shown in the top panel. Density is shown in black contours. The dashed red line denotes the mixed layer depth.

surrounding Gulf Stream. The large straining on the upstream side of a trough meander is a generic feature of the Gulf Stream meanders before or after separation. Observations of Gulf Stream meanders have shown that a frontal jet tends to be confluent and frontogenetic on the upstream side of a meander trough and diffluent and frontolytic on the downstream side of a meander trough (Bower 1989; Thomas and Joyce 2010).

The advective frontal tendency, that is, the rate of change of the amplitude of the buoyancy gradient

following a fluid parcel due to the horizontal advection, is defined as in Hoskins (1982) by

$$T_{\text{adv}} = \frac{1}{2} \frac{D \|\nabla_h b\|^2}{Dt} = (-b_x \nabla_h u - b_y \nabla_h v) \cdot \nabla_h b, \quad (1)$$

where $b = -g(\rho/\rho_0)$ is the buoyancy, ρ is the in situ density, ρ_0 is the mean reference density, and g is the gravitational acceleration. The frontal tendency is strongly positive on the upstream face of the trough and mostly negative on the downstream face with smaller-scale

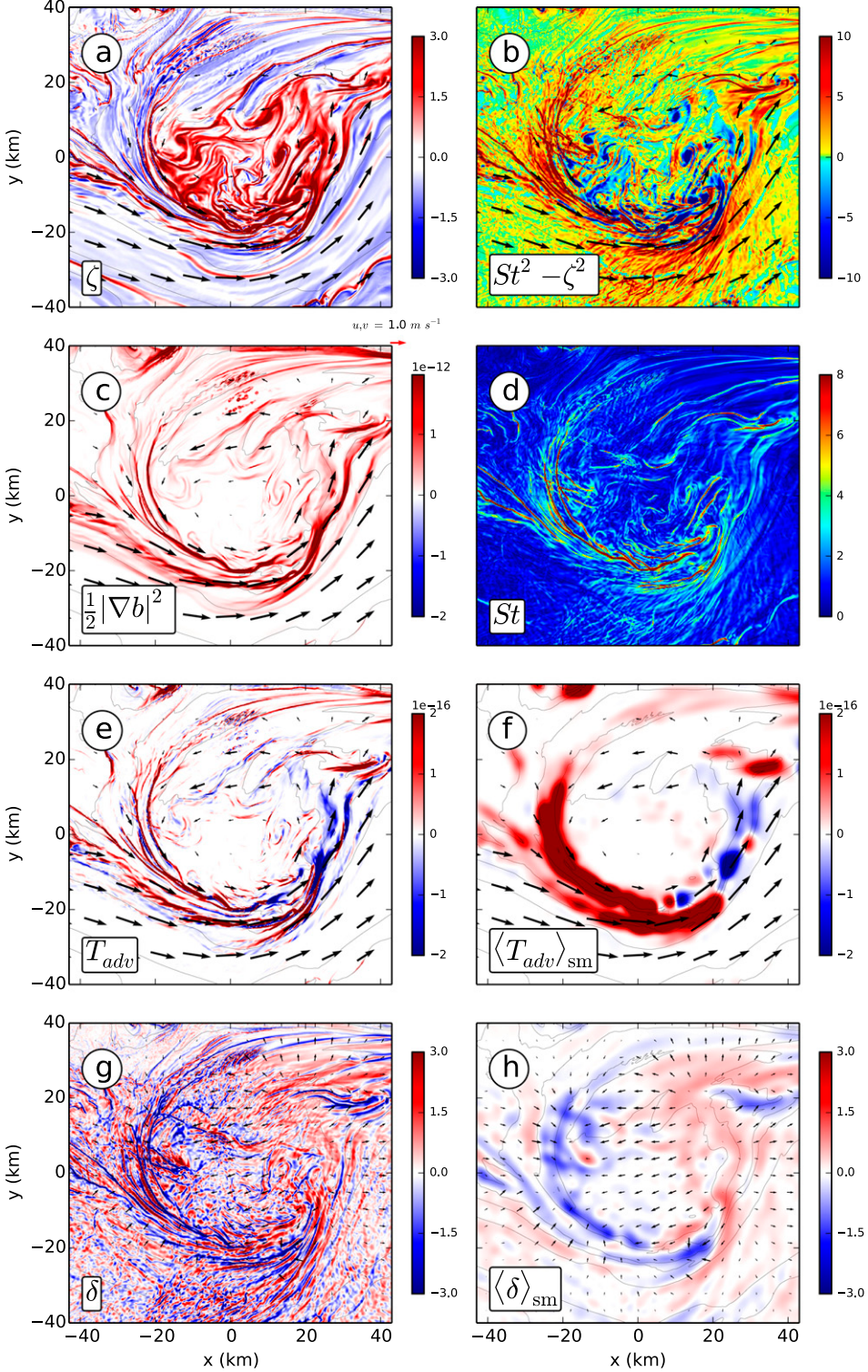


FIG. 10. Instantaneous horizontal patterns for the frontal eddy at $z = -10$ m for the frontal eddy of Fig. 8: (a) relative vorticity $\zeta = v_x - u_y$, normalized by f ; (b) Okubo–Weiss parameter $St^2 - \zeta^2$, normalized by f^2 ; (c) frontal sharpness $0.5||\nabla b||^2$ (i.e., variance of the horizontal density gradient); (d) horizontal strain rate $St = \sqrt{(u_x - v_y)^2 + (v_x + u_y)^2}$, normalized by f ; and (e),(f) frontal sharpness tendency due to 3D advection T_{adv} and (g),(h) divergence $\delta = u_x + v_y$, normalized by f . (f) and (h) are horizontally smoothed by using a convolution with a Gaussian kernel of half-width 5 km. Buoyancy is shown in thin black contours with an interval of $2.5 \times 10^{-3} \text{ m s}^{-2}$. Black vectors in (a) and (g) and (h) show the nondivergent part and the divergent part of the flow, respectively, while the black vectors in (b), (c), (d), (e), and (f) show the total velocity field.

fluctuations related to small-scale meandering of the fronts (Figs. 10e,f). These spatial relationships are all consistent with frontogenesis on the upstream face, triggered by the straining of the horizontal flow, and sharpening of the horizontal cross-front buoyancy gradients between the upstream and downstream sides of the trough meander. The straining is weakened on the downstream face where cross-front perturbations are growing and the front starts meandering.

The divergence of the flow is dominated by very intense small-scale patterns (Fig. 10g). The divergence signals in the frontal zone are mostly due to the secondary circulation associated with the frontogenesis of the multiple fronts and filaments. The frontal region is also a potential source for spontaneously emitted inertia–gravity waves (Danioux et al. 2012; Shakespeare and Taylor 2014; Nagai et al. 2015), as the flow departs significantly from geostrophic balance in the frontogenetic region, where vorticity values in the submesoscale features can locally reach values up to 50–100 f . The divergence signals due to the waves are not easily distinguishable from the divergence signals associated with the frontogenesis, which in both cases have similar horizontal scales. The intense small-scale divergence signals in the Gulf Stream away from the frontal zone and parallel to the downstream face of the meander trough (Fig. 10g) have characteristics of internal gravity waves. The localized emission is consistent with the fact that waves may be trapped by the oncoming straining flow and can only propagate away from the frontal zone where the straining is weakened (Shakespeare and Taylor 2014). The horizontally smoothed divergence signal (Fig. 10h) exhibits the characteristic positive–negative signature corresponding to upwelling on the leading edge of the cold dome and downwelling on the trailing edge as seen previously (Fig. 5).

b. Formation of submesoscale vortices

The meandering of the front on the downstream face of the trough is an indication of a submesoscale instability of the front. A sequence of density and vorticity snapshots showing the evolution of the frontal eddy around the time of Fig. 6a is shown in Fig. 11. Lagrangian particles have been seeded at the surface in a high vorticity filament ($\zeta > 10f$) at the time of Fig. 11a to help visualize the life cycle of vorticity filaments during the instability process. The sequence shows the front on the downstream face becoming unstable, expressed in the meandering of the vorticity filament associated with the front. The small-scale meanders have a wavelength of about 20 km. The vorticity filament breaks up into a string of submesoscale vortices that are advected into the interior of the eddy to form

the submesoscale structures evident in Fig. 9. These small-scale vorticity structures are then advected back in the high strain region on the upstream face of the trough and follow the same cycle again, ultimately leading to the more complicated pattern shown in Fig. 10. This sequence—shown here at an early stage after the formation of the frontal eddy, such that the structure of the eddy is initially relatively simple (Fig. 11a)—is repeated during the whole lifetime of the frontal eddy.

To identify the nature of the instability processes that generate the vortices, it is useful to look at the source of eddy energy. We compute the kinetic energy conversion terms between the curved parallel flow and its meandering perturbations in a local reference frame aligned with the front following the methodology described in Gula et al. (2014). The local coordinates are x and y in the along- and cross-front direction, respectively, and the corresponding horizontal velocities u and v . For this analysis the local mean, denoted by an overbar, is defined as the alongfront average for the region considered. Perturbations relative to that mean are denoted with a prime such that the total field of any quantity can be written as $b = \bar{b} + b'$, $u = \bar{u} + u'$, $v = \bar{v} + v'$, and so on. An example of such a decomposition for buoyancy is shown in Fig. 12 at the time and location of Fig. 11b.

Energy conversion terms are computed following Harrison and Robinson (1978). The mean kinetic to eddy kinetic energy conversion, which can be divided into contributions from the horizontal Reynolds stress (HRS) and the vertical Reynolds stress (VRS), is written as

$$K_m K_e = \text{HRS} + \text{VRS}, \quad (2)$$

where

$$\text{HRS} = -\bar{u}'^2 \frac{\partial \bar{u}}{\partial x} - \bar{u}' \bar{v}' \frac{\partial \bar{u}}{\partial y} - \bar{v}'^2 \frac{\partial \bar{v}}{\partial y} - \bar{u}' \bar{v}' \frac{\partial \bar{v}}{\partial x} \quad (3)$$

corresponds to the product of horizontal mean shear and horizontal Reynolds stress, and

$$\text{VRS} = -\bar{u}' w' \frac{\partial \bar{u}}{\partial z} - \bar{v}' w' \frac{\partial \bar{v}}{\partial z} \quad (4)$$

arises from vertical shear of the mean flow and vertical Reynolds stress. The eddy potential to eddy kinetic energy conversion is the vertical eddy buoyancy flux (VBF):

$$P_e K_e = \text{VBF} = \overline{w' b'}, \quad (5)$$

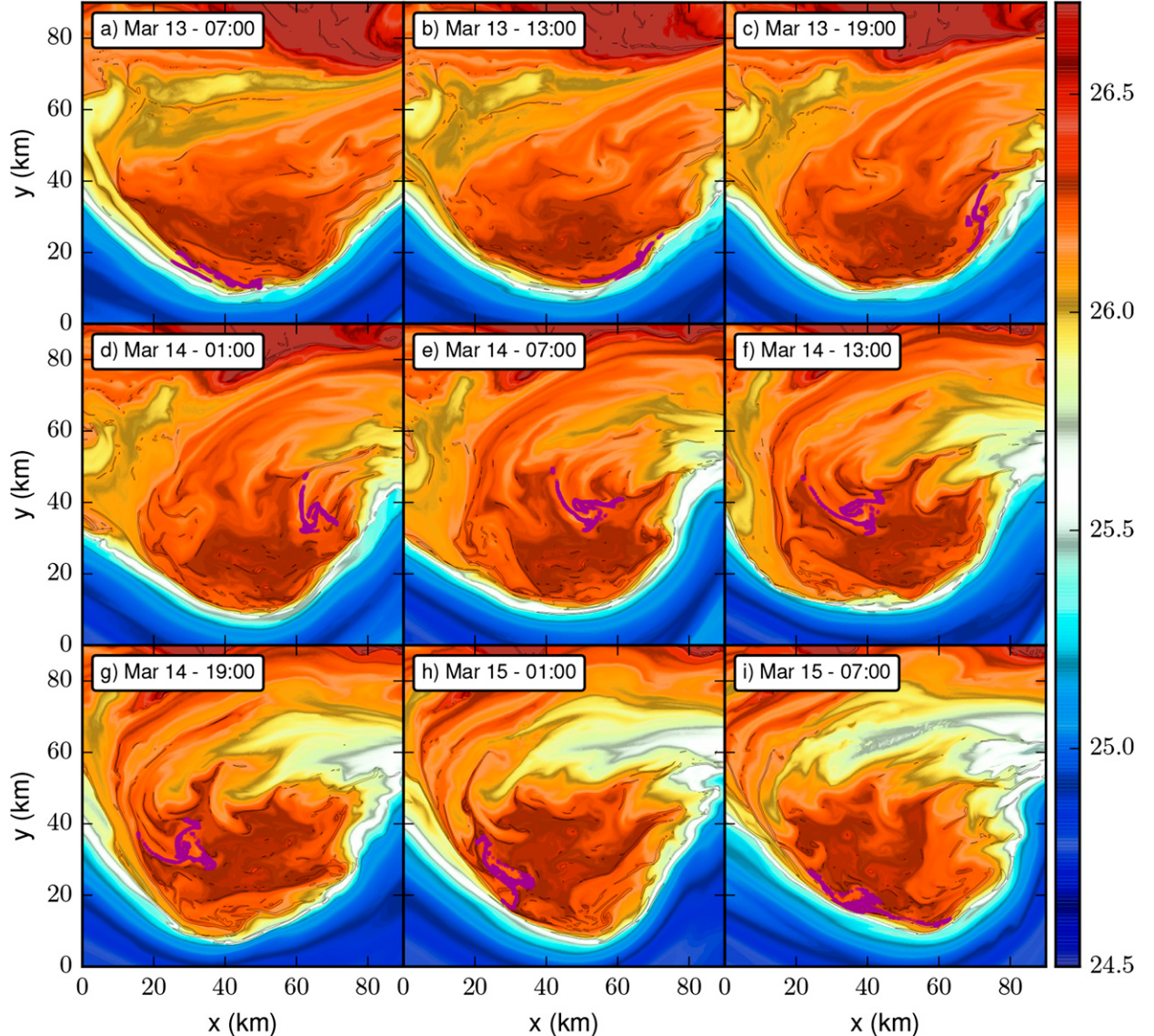


FIG. 11. Sequence of snapshots of density at $z = -10$ m (kg m^{-3} ; colors) and relative vorticity (at $\pm 4f$ in black contours) for the frontal eddy every 6 h, showing the early stages of the instability and the formation of intrafrontal-eddy submesoscale vortices. The magenta dots are Lagrangian particles seeded at the surface in a vorticity filament ($\zeta > 10f$) at the time of (a) to help visualizing the life cycle of vorticity filaments during the instability process.

where b is the buoyancy anomaly relative to the local area average.

Predominance of one of the three source terms indicates that the eddy generation mechanism is primarily: a baroclinic instability ($\text{VBF} = \overline{w'b'} > 0$), a barotropic instability ($\text{HRS} > 0$), or a vertical shear (Kelvin-Helmholtz type) instability ($\text{VRS} > 0$). The alongfront-averaged kinetic energy conversion terms, vertically integrated over the upper 200 m, are shown in Fig. 12b. The HRS term, conversion from mean kinetic energy to eddy kinetic energy through horizontal Reynolds stress, is the dominant term. Other sources like the baroclinic term

VBF and the vertical shear stress VRS are small. The energy source for the perturbations is the horizontal shear of the mean flow. The vertical structure of the HRS term shows that it is surface intensified and disappears below 50 m (Fig. 12d). The meander-induced frontogenesis sharpens the gradients on the upstream face of the trough, in particular the cross-front velocity shear u_y , and triggers submesoscale barotropic shear instability of the front in the sector where the strain rate is not quite so large.

Following the classic analysis by Rayleigh (1880), an isolated two-dimensional vorticity filament is always

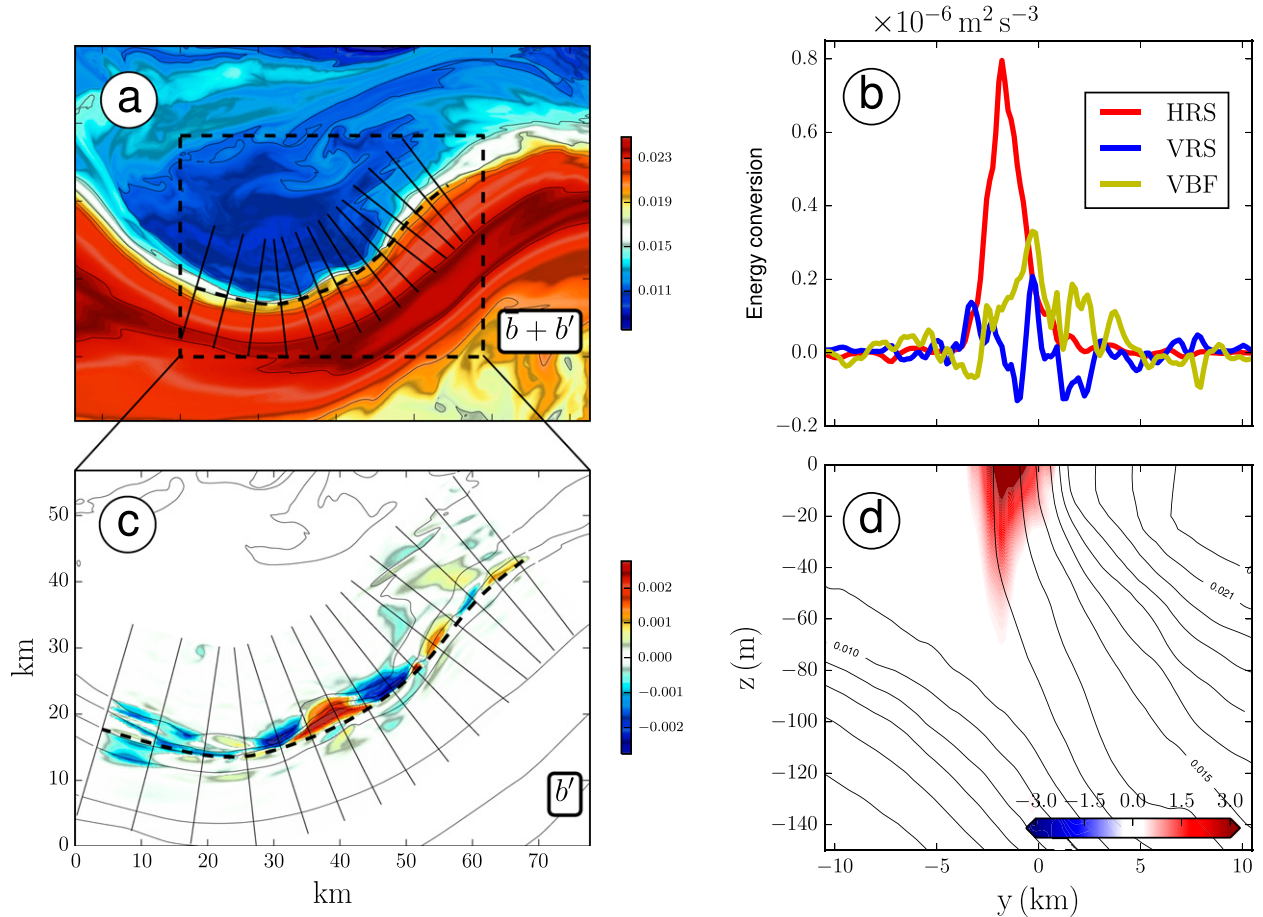


FIG. 12. (a) Total surface buoyancy field b with a black dashed line marking the alongfront axis and black solid lines individual cross sections and (c) perturbation field b' after subtracting the alongfront mean profile for the frontal eddy at the time of Fig. 11b. (b) Instantaneous local energy conversions profiles HRS, VRS, and VBF averaged in the alongfront direction and over the upper 200 m and (d) vertical section of HRS averaged in the alongfront direction. The unit of the eddy conversion terms is $10^{-6} \text{ m}^2 \text{s}^{-3}$.

unstable and expected to roll up into discrete vortices. However, the presence of a background strain can stabilize the horizontal shear instability of a vorticity filament (Dritschel et al. 1991). A schematic summary of the submesoscale phenomena is shown in Fig. 13. The strong straining acts to sharpen the velocity gradient as well as stabilizing the barotropic shear instability on the upstream face of the trough. The strain weakens in the trough, the cross-front perturbations are allowed to grow, and the front becomes unstable. The small-scale meandering perturbations ultimately evolve into rolled-up vortices that are advected back into the interior of the frontal eddy as seen in the time sequence of Fig. 9.

c. Diabatic mixing by submesoscale processes

To identify the origin of the water in the low-salinity surface intrusions created by the submesoscale vortices, virtual Lagrangian particles are deployed in the model

solutions and are advected backward in time. The particles are neutrally buoyant Lagrangian (flow following) particles, and they are advected by the model velocity fields without any additional dispersion from the model's mixing processes. A fourth-order Runge–Kutta method with a small time step size $dt = 1\text{ s}$ is used to compute particle advection. Velocity and tracer fields are interpolated at the positions of the particles using cubic spline interpolation in both the horizontal and vertical directions. We use hourly averaged outputs from the simulation to get sufficiently frequent and temporally smooth velocity sampling for accurate parcel advection.

Particles are seeded in the low-salinity surface intrusions ($z > -40\text{ m}$ and $S < 36.13\text{ psu}$) at the time t_s of Fig. 9. The distribution of particles at t_s is shown in Figs. 14a and 14b. Density and depth variations following the particles are shown in Figs. 14c and 14d, respectively, for the previous 200 h.

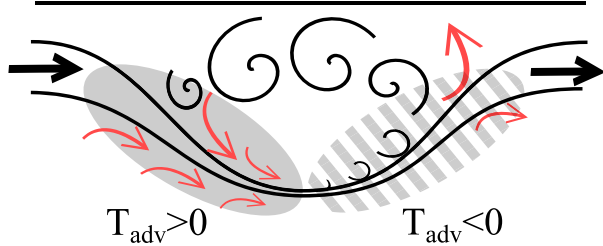


FIG. 13. Schematic diagram for the meander-induced frontogenesis, barotropic shear instability, and formation of submesoscale vortices in the propagating trough enclosing the frontal eddy. Black lines show isolines of vorticity and tracers. Perturbations are strain elongated on the left, meandering in the lower middle, and rolled up vortices on the right. The plain and dashed gray filled area show the positive and negative frontal tendency regions induced by the mesoscale straining of the flow.

Three main groups of particles can be identified depending on their original density (Fig. 14): the particles from the upper part of the eddy, which did not undergo any significant density change p_1 ; the heavy, cold, and fresh particles from the upwelled cold core of the eddy p_2 ; and the light, warm, and salty particles from the Gulf Stream core p_3 .

Particles p_1 have a density of $26.2 < \rho < 26.3 \text{ kg m}^{-3}$ throughout the simulation. They are visible as black lines in Fig. 14c. There is a small positive trend in the evolution of their density directly related to the strong cooling at the surface of the ocean at this time of the year (end of winter). Particles p_1 revolve around the center of the frontal eddy and move adiabatically along isopycnals. The isopycnals are sloped in the cross-shelf direction such that particles undergo large-amplitude vertical displacements during each eddy revolution. Vertical displacements can reach 150–200 m and have a 2-day periodicity (Fig. 14d). This corresponds to mean vertical velocities values $\approx \pm 2 \text{ mm s}^{-1}$, in agreement with the amplitudes of the instantaneous vertical velocities at $z = -200 \text{ m}$ in the frontal eddy plotted in Fig. 5. The vertical velocities associated with the upwelling, corresponding to the uplifting of the isopycnals, can be estimated by looking at the variation of the depths of the particles averaged over each period of revolution of the eddy. Vertical velocities in the range of $5\text{--}10 \text{ m day}^{-1}$, an order of magnitude smaller than instantaneous vertical velocities, can be estimated from Fig. 14d.

The variations of temperature and salinity for a Lagrangian particle in our model are due to either horizontal diffusion or vertical mixing. The vertical mixing rate for salinity, that is, $(\partial/\partial z)[K_{sv}(\partial S/\partial z)]$, where the tracer mixing coefficient K_{sv} is computed using KPP (Large et al. 1994) is plotted in Figs. 14e and 14f in the horizontal and vertical planes centered around the mean position of the particles at the time

t_m . The strong salinity variations that particles undergo are almost entirely due to the vertical mixing term in the vicinity of the frontogenetic region. Temperature variations along particle trajectories are similarly controlled by the vertical mixing term (not shown).

The warm, salty, and light particles from the Gulf Stream p_3 cross the front and get into the eddy core in the upper surface layer ($z > -50 \text{ m}$) where the vertical mixing term for tracers is negative (see violet arrows in Figs. 14c,f). The DT/Dt and DS/Dt are $\approx -2 \times 10^{-4} \text{ K s}^{-1}$ and $\approx -0.05 \times 10^{-4} \text{ psu s}^{-1}$, respectively, in the upper 80 m at the time of Fig. 14f. These values are consistent with the observed change of $\Delta T = -4 \text{ K}$ and $\Delta S = -0.1 \text{ psu}$ in a 5-h span (Fig. 14c). The impact of the horizontal diffusion on the transformations described here is several orders of magnitude smaller than the effect of the vertical mixing.

The heavy, cold, and fresh particles from the upwelled cold core of the eddy p_2 also undergo large changes in the vicinity of the frontogenetic region at depths between -150 and -100 m (see golden arrows in Figs. 14c,f). The mixed layer depth is defined here as the layer of active mixing resulting from the KPP scheme. It reaches locally $z = -180 \text{ m}$ because of the weak stratification and strong vertical velocity shear at the center of the front. Particles p_2 , while moving up along the sloped isopycnals, cross the deep part of the front (Fig. 14f), where the vertical mixing terms for temperature and salinity are positive and where they lighten in density.

The deep front on the rim of the eddy, which extends into the pycnocline, dynamically couples the mixed layer and pycnocline. It enhances exchanges of buoyancy and tracers between the mixed layer and the interior, as also observed in the idealized experiments of Ramachandran et al. (2014).

d. Potential vorticity structure, boundary vorticity generation, and centrifugal instability

The topographic drag against the slope is a source of relative vorticity and potential vorticity. A boundary slope current moving anticyclonically/cyclonically around a basin (meaning that the flow has the coast on its left/right in the Northern Hemisphere) can generate highly positive/negative relative vorticity and potential vorticity values within the sloped turbulent bottom boundary layer. The interaction of the Gulf Stream with the continental slope on its cyclonic side leads to injection of positive relative vorticity and potential vorticity in the interior (Gula et al. 2015b). For boundary slope currents moving cyclonically around a basin, as demonstrated in the case of the California Undercurrent (Molemaker et al. 2015), the topographic drag amplifies the anticyclonic shear and

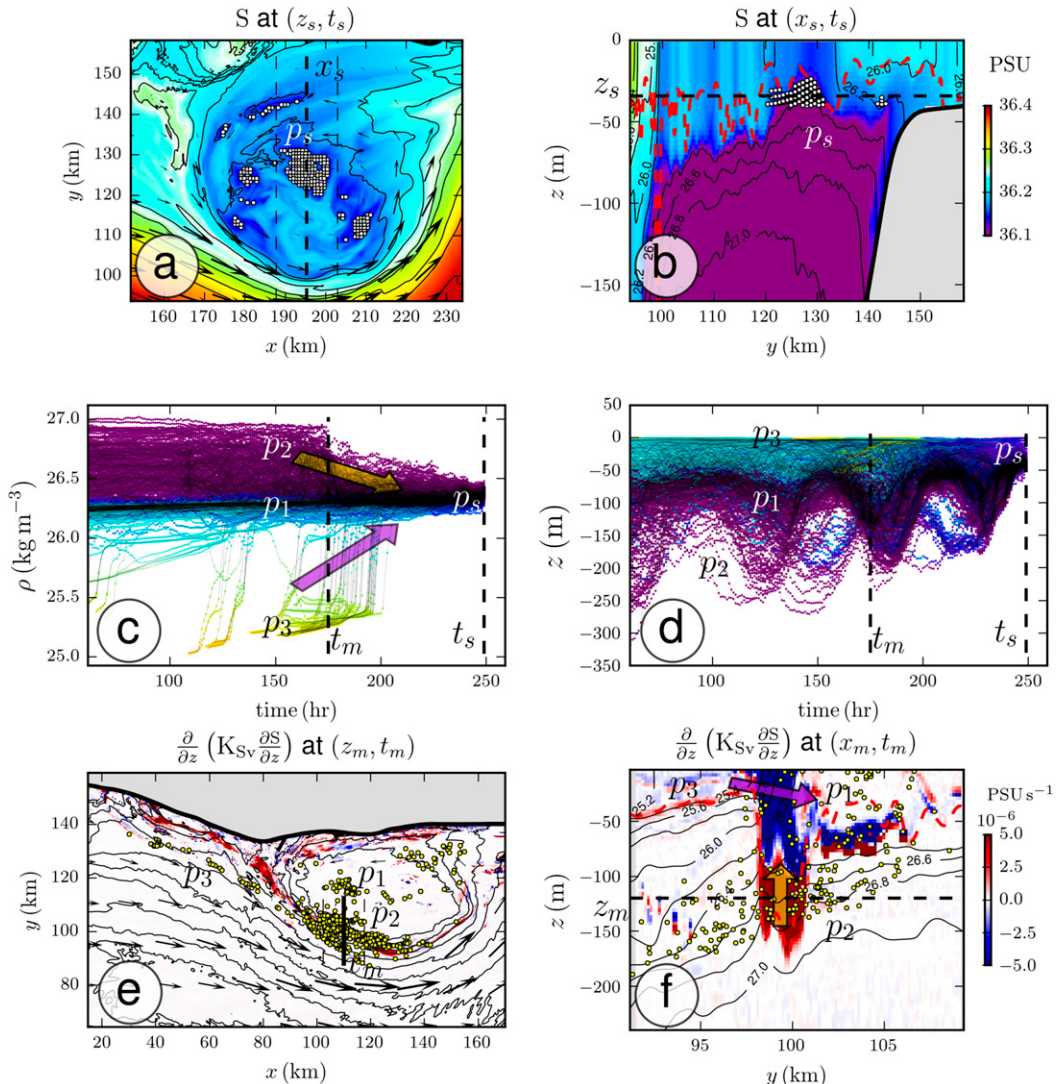


FIG. 14. (a) horizontal section at the mean depth z_s of the particles and (b) vertical section in the cross-shelf direction showing salinity (colors), density (black contours), velocity (vectors), and particle positions (white dots) at the time of particle seeding ($t_s = 250$ h). (c) Density and (d) depth evolution of the particles with time. Colors show the salinity of the particles at the corresponding position using the same color scale as in the top panels. (e) Instantaneous vertical salinity mixing tendency term $\{\frac{\partial}{\partial z}\}[K_{Sv} \frac{\partial S}{\partial z}]\}, \text{psu s}^{-1}\}$ in the horizontal and (f) vertical planes centered on the mean position of the plotted ensemble of particles (marked as yellow dots) at time $t_m = t_s - 70$ h. Black contours show density. The dashed red line denotes the mixed layer depth. The violet and golden arrows in (c) and (f) show the mean trajectories in density and space of the particle groups p_3 and p_2 , respectively, which undergo significant density changes during the simulation. For clarity, only 4% of the total number of particles is plotted.

generates large negative relative vorticity and potential vorticity values.

The frontal eddy locally generates a strong southward flow against the continental slope. Following the sequence of processes described in Molemaker et al. (2015), relative vorticity can locally become much less than $-f$ and potential vorticity becomes negative, which is a criterion for ageostrophic centrifugal instability (Hoskins 1974). Centrifugal instability gives rise to unbalanced submesoscale

turbulence with elevated local energy dissipation and mixing. Figure 15 shows horizontal and vertical sections of potential vorticity at the location of the frontal eddy of Fig. 10, where potential vorticity q is defined as

$$q = \boldsymbol{\omega}_a \cdot \nabla b, \quad (6)$$

with $\boldsymbol{\omega}_a = f\mathbf{z} + \nabla \times \mathbf{u}$ as the absolute vorticity vector, \mathbf{z} the vertical unit vector, and \mathbf{u} the velocity.

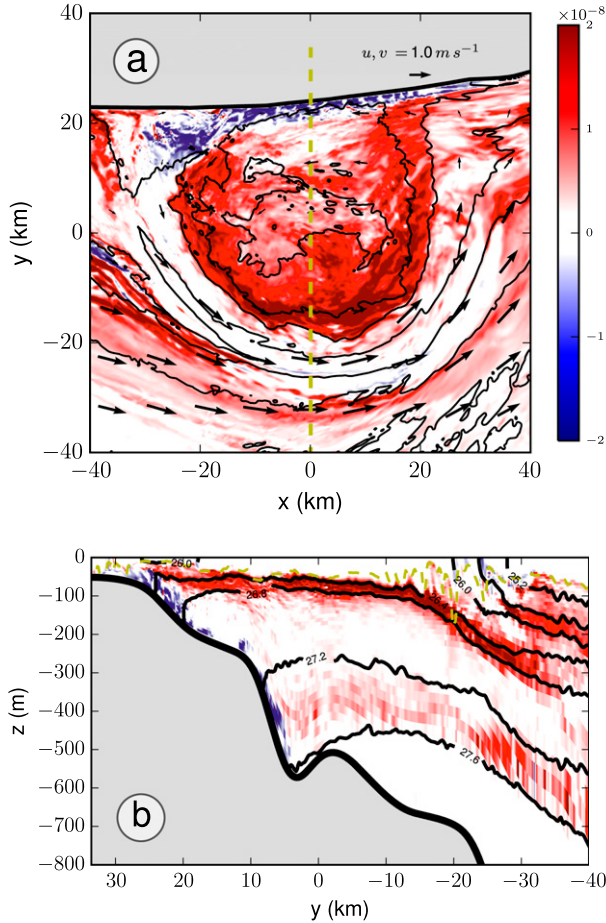


FIG. 15. (a) Horizontal section at $z = -100$ m and (b) vertical section of potential vorticity q (colors) and density (black contours) at the center of the frontal eddy plotted in Fig. 10 along the cross-stream direction y . The dashed yellow line in (b) denotes the mixed layer depth. Notice in particular the negative potential vorticity created by drag from the southward frontal eddy flow along the slope and the collar of positive potential vorticity at the base of the mixed layer created by penetrative vertical mixing entrainment, some of which is advected isopycnally into the interior.

The potential vorticity structure points out two potential local sources of potential vorticity, namely, the boundary stress input due to the drag on the flow over the slope (Gula et al. 2015b) and the vertical mixing at the base of the mixed layer that enhances the vertical buoyancy gradient there. The strong negative potential vorticity values near the slope instigate ageostrophic centrifugal instability and are quickly mixed away in the model by a combination of the parameterized mixing and resolved flow response. The values of the salinity mixing tendency term near the slope (Fig. 14e), where negative potential vorticity is generated, are indicative of the response of the vertical mixing parameterization (KPP), which represents in the ocean interior the parameterization of small Richardson number

processes and static instabilities. A large positive potential vorticity region exists at the base of the mixed layer, around $z = -100$ m, due to the maximum in density stratification there, and some of this is then advected isopycnally into the interior by the frontal eddy circulation. The other positive potential vorticity region is seen deeper (around $z = -500$ m). It corresponds to the bottom drag generation of potential vorticity associated with the drag of northward Gulf streamflow along the slope upstream of this section (where it is seen at the bottom, but here it has been upwelled inside the trough meander during the formation of the frontal eddy). Thus, potential vorticity is highly nonconservative within the Gulf Stream along the seaboard due to boundary flux and mixing processes.

6. Summary and conclusions

In this study, we address the behavior of a Gulf Stream frontal eddy after the formation over the Charleston Bump. The characteristics of the frontal eddy demonstrated here are typical for the frontal eddies that are generated in our simulations and for numerous examples of frontal eddies observed in the SAB region. The frontal eddy cross- and alongshore scales are about 50 and 100 km, respectively, and the frontal eddy propagates downstream with a velocity of about 25 km day^{-1} . During its propagation, between the Bump and Cape Hatteras, the frontal eddy progressively becomes smaller and weaker as the slope becomes steeper, and the eddy is ultimately sheared apart in the vicinity of Cape Hatteras.

We compare results from identical simulations with different horizontal resolutions ($\Delta x \approx 1.5 \text{ km}$, $\Delta x \approx 500 \text{ m}$, and $\Delta x \approx 150 \text{ m}$) and find that there are important differences in the structure of the frontal eddy between them. The frontal eddy decay in the $\Delta x \approx 1.5 \text{ km}$ solution is more pronounced as it propagates along the shelf downstream from the bump, and it accelerates faster than in the higher-resolution nested grids. The upwelling in the cold core of the eddy is intensified when the resolution is increased. In the highest-resolution nest, there are submesoscale patterns that create localized regions of intense upwelling bringing additional cold and freshwater from the upwelled cold of the eddy inside the surface mixed layer.

The submesoscale structures that emerge in the interior of the frontal eddy are cyclonic vortices. Diagnostics show submesoscale strain-induced frontogenesis acting on the edge of the eddy. The strong meander-induced straining acts to sharpen the velocity gradient as well as stabilize the barotropic shear instability on the upstream face of the trough meander that forms the boundary between the frontal eddy and the adjacent Gulf Stream. The strain weakens in the

trough, the cross-front perturbations are allowed to grow with lateral Reynolds stress conversion as the local eddy energy source, and the front becomes unstable. The small-scale meandering perturbations ultimately become rolled-up vortices that are advected back in the interior of the frontal eddy.

The deep front on the rim of the eddy enhances mixing and tracer transport from the interior into the mixed layer. This enhancement of tracer transport at deep fronts has implications for the exchange of nutrients and biogeochemical tracers between the interior and the surface mixed layer.

Potential vorticity is highly nonconservative within the Gulf Stream along the seaboard due to boundary flux and mixing processes. In particular, the frontal eddy locally creates a strong reversal (southward) current against the slope, leading to negative potential vorticity generation by bottom drag. The negative values of potential vorticity trigger centrifugal instability and generate unbalanced submesoscale turbulence that has elevated local dissipation and mixing.

Simulations with a horizontal resolution of $\Delta x \approx 1.5$ km, which are usually considered as a high standard in numerical modeling for realistic oceanographic studies, are not able to reproduce the submesoscale features of the frontal eddy. The frontogenesis is weaker on the rim of the eddy, and the front is not sharp enough to become unstable to horizontal shear instability. The frontogenetic region is shallower and the tracer mixing and exchanges between the interior and the mixed layer are weaker than in the higher-resolution simulations. The mesoscale properties of the eddy are also altered in the lower-resolution simulation with a faster decay of the eddy, a larger acceleration as it propagates along the shelf, and a significant weakening of the intensity of the upwelling in the core of the eddy.

The upwelling of nutrient-rich water in the core of frontal eddies is an important factor for the production of phytoplankton and zooplankton (Yoder et al. 1981; McClain and Atkinson 1985; Lee et al. 1991). The submesoscale dynamics described here could potentially impact the biological production in the South Atlantic Bight by further increasing the supply of nutrients in the surface layer, with a further local enhancement inside the submesoscale vortices.

It is clear from this and recent related studies of the Gulf Stream that it has very active submesoscale frontal and eddy dynamics, which are geographically variable and distinct from midoceanic submesoscale behaviors. The submesoscale is also an integral part of the interaction of the Gulf Stream over the continental slope with the adjacent shelf currents and material distributions. While much is being learned about this unfamiliar

dynamical regime, no doubt further surprises lie ahead. As yet we are not able to say in general just how much submesoscale eddy fluxes modify the Gulf Stream and its mesoscale variability, but the examples of local instability and mixing presented here are steps toward that goal.

Acknowledgments. We appreciate support from the Office of Naval Research (N00014-12-1-0939, N00014-12-1-0105) and the National Science Foundation (OCE-1049134). The altimeter products were produced by Ssalto/Duacs and distributed by AVISO, with support from CNES (<http://www.aviso.altimetry.fr/duacs/>).

REFERENCES

- Bane, J., Jr., and W. Dewar, 1988: Gulf Stream bimodality and variability downstream of the Charleston Bump. *J. Geophys. Res.*, **93**, 6695–6710, doi:[10.1029/JC093iC06p06695](https://doi.org/10.1029/JC093iC06p06695).
- , D. Brooks, and K. Lorenson, 1981: Synoptic observations of the three-dimensional structure and propagation of Gulf Stream meanders along the Carolina continental margin. *J. Geophys. Res.*, **86**, 6411–6425, doi:[10.1029/JC086iC07p06411](https://doi.org/10.1029/JC086iC07p06411).
- Blanton, J., L. Atkinson, L. Pietrafesa, and T. Lee, 1981: The intrusion of Gulf Stream water across the continental shelf due to topographically-induced upwelling. *Deep-Sea Res.*, **28**, 393–405, doi:[10.1016/0198-0149\(81\)90006-6](https://doi.org/10.1016/0198-0149(81)90006-6).
- Boccaletti, G., R. Ferrari, and B. Fox-Kemper, 2007: Mixed layer instabilities and restratification. *J. Phys. Oceanogr.*, **37**, 2228–2250, doi:[10.1175/JPO3101.1](https://doi.org/10.1175/JPO3101.1).
- Bower, A. S., 1989: Potential vorticity balances and horizontal divergence along particle trajectories in Gulf Stream meanders east of Cape Hatteras. *J. Phys. Oceanogr.*, **19**, 1669–1681, doi:[10.1175/1520-0485\(1989\)019<1669:PVBAHD>2.0.CO;2](https://doi.org/10.1175/1520-0485(1989)019<1669:PVBAHD>2.0.CO;2).
- Bracco, A., and J. Pedlosky, 2003: Vortex generation by topography in locally unstable baroclinic flows. *J. Phys. Oceanogr.*, **33**, 207–219, doi:[10.1175/1520-0485\(2003\)033<0207:VGBTIL>2.0.CO;2](https://doi.org/10.1175/1520-0485(2003)033<0207:VGBTIL>2.0.CO;2).
- Brooks, D., and J. Bane Jr., 1981: Gulf Stream fluctuations and meanders over the Onslow Bay upper continental slope. *J. Phys. Oceanogr.*, **11**, 247–256, doi:[10.1175/1520-0485\(1981\)011<0247:GSFAMO>2.0.CO;2](https://doi.org/10.1175/1520-0485(1981)011<0247:GSFAMO>2.0.CO;2).
- , and —, 1983: Gulf Stream meanders off North Carolina during winter and summer 1979. *J. Geophys. Res.*, **88**, 4633–4650, doi:[10.1029/JC088iC08p04633](https://doi.org/10.1029/JC088iC08p04633).
- Carton, J., and B. Giese, 2008: A reanalysis of ocean climate using Simple Ocean Data Assimilation (SODA). *Mon. Wea. Rev.*, **136**, 2999–3017, doi:[10.1175/2007MWR1978.1](https://doi.org/10.1175/2007MWR1978.1).
- Danioux, E., J. Vanneste, P. Klein, and H. Sasaki, 2012: Spontaneous inertia-gravity-wave generation by surface-intensified turbulence. *J. Fluid Mech.*, **699**, 153–173, doi:[10.1017/jfm.2012.90](https://doi.org/10.1017/jfm.2012.90).
- Dewar, W., and J. Bane Jr., 1985: Subsurface energetics of the Gulf Stream near the Charleston Bump. *J. Phys. Oceanogr.*, **15**, 1771–1789, doi:[10.1175/1520-0485\(1985\)015<1771:SEOTGS>2.0.CO;2](https://doi.org/10.1175/1520-0485(1985)015<1771:SEOTGS>2.0.CO;2).
- Dritschel, D., P. Haynes, M. Juckes, and T. Shepherd, 1991: The stability of a two-dimensional vorticity filament under uniform strain. *J. Fluid Mech.*, **230**, 647–665, doi:[10.1017/S0022112091000915](https://doi.org/10.1017/S0022112091000915).

- Glenn, S., and C. Ebbesmeyer, 1994: The structure and propagation of a Gulf Stream frontal eddy along the North Carolina shelf break. *J. Geophys. Res.*, **99**, 5029–5046, doi:[10.1029/93JC02786](https://doi.org/10.1029/93JC02786).
- Govoni, J., J. Hare, and E. Davenport, 2013: The distribution of larval fishes of the Charleston Gyre region off the southeastern United States in winter shaped by mesoscale, cyclonic eddies. *Mar. Coastal Fish.*, **5**, 246–259, doi:[10.1080/19425120.2013.820245](https://doi.org/10.1080/19425120.2013.820245).
- Gula, J., M. Molemaker, and J. McWilliams, 2014: Submesoscale cold filaments in the Gulf Stream. *J. Phys. Oceanogr.*, **44**, 2617–2643, doi:[10.1175/JPO-D-14-0029.1](https://doi.org/10.1175/JPO-D-14-0029.1).
- , —, and —, 2015a: Gulf Stream dynamics along the southeastern U.S. seaboard. *J. Phys. Oceanogr.*, **45**, 690–715, doi:[10.1175/JPO-D-14-0154.1](https://doi.org/10.1175/JPO-D-14-0154.1).
- , —, and —, 2015b: Topographic vorticity generation, submesoscale instability and vortex street formation in the Gulf Stream. *Geophys. Res. Lett.*, **42**, 4054–4062, doi:[10.1002/2015GL063731](https://doi.org/10.1002/2015GL063731).
- Haney, J., 1986: Seabird segregation at Gulf Stream frontal eddies. *Mar. Ecol. Prog. Ser.*, **28**, 279–285, doi:[10.3354/meps028279](https://doi.org/10.3354/meps028279).
- Harrison, D., and A. Robinson, 1978: Energy analysis of open regions of turbulent flows: Mean eddy energetics of a numerical ocean circulation experiment. *Dyn. Atmos. Oceans*, **2**, 185–211, doi:[10.1016/0377-0265\(78\)90009-X](https://doi.org/10.1016/0377-0265(78)90009-X).
- Hoskins, B. J., 1974: The role of potential vorticity in symmetric stability and instability. *Quart. J. Roy. Meteor. Soc.*, **100**, 480–482, doi:[10.1002/qj.49710042520](https://doi.org/10.1002/qj.49710042520).
- , 1982: The mathematical theory of frontogenesis. *Annu. Rev. Fluid Mech.*, **14**, 131–151, doi:[10.1146/annurev.fl.14.010182.001023](https://doi.org/10.1146/annurev.fl.14.010182.001023).
- Large, W., J. McWilliams, and S. Doney, 1994: Oceanic vertical mixing: A review and a model with a nonlocal boundary layer parameterization. *Rev. Geophys.*, **32**, 363–403, doi:[10.1029/94RG01872](https://doi.org/10.1029/94RG01872).
- Lee, T., and L. Atkinson, 1983: Low-frequency current and temperature variability from Gulf Stream frontal eddies and atmospheric forcing along the southeast U.S. outer continental shelf. *J. Geophys. Res.*, **88**, 4541–4567, doi:[10.1029/JC088iC08p04541](https://doi.org/10.1029/JC088iC08p04541).
- , —, and R. Legeckis, 1981: Observations of a Gulf Stream frontal eddy on the Georgia continental shelf, April 1977. *Deep-Sea Res.*, **28**, 347–378, doi:[10.1016/0198-0149\(81\)90004-2](https://doi.org/10.1016/0198-0149(81)90004-2).
- , J. Yoder, and L. Atkinson, 1991: Gulf Stream frontal eddy influence on productivity of the southeast U.S. continental shelf. *J. Geophys. Res.*, **96**, 22 191–22 205, doi:[10.1029/91JC02450](https://doi.org/10.1029/91JC02450).
- Legeckis, R., 1975: Application of synchronous meteorological satellite data to the study of time dependent sea surface temperature changes along the boundary of the Gulf Stream. *Geophys. Res. Lett.*, **2**, 435–438, doi:[10.1029/GL002i010p00435](https://doi.org/10.1029/GL002i010p00435).
- , 1979: Satellite observations of the influence of bottom topography on the seaward deflection of the Gulf Stream off Charleston, South Carolina. *J. Phys. Oceanogr.*, **9**, 483–497, doi:[10.1175/1520-0485\(1979\)009<0483:SOOTIO>2.0.CO;2](https://doi.org/10.1175/1520-0485(1979)009<0483:SOOTIO>2.0.CO;2).
- McClain, C., and L. Atkinson, 1985: A note on the Charleston Gyre. *J. Geophys. Res.*, **90**, 11 857–11 861, doi:[10.1029/JC090iC06p11857](https://doi.org/10.1029/JC090iC06p11857).
- , L. Pietrafesa, and J. Yoder, 1984: Observations of Gulf Stream-induced and wind-driven upwelling in the Georgia Bight using ocean color and infrared imagery. *J. Geophys. Res.*, **89**, 3705–3723, doi:[10.1029/JC089iC03p03705](https://doi.org/10.1029/JC089iC03p03705).
- Molemaker, M., J. McWilliams, and W. Dewar, 2015: Submesoscale instability and generation of mesoscale anticyclones near a separation of the California Undercurrent. *J. Phys. Oceanogr.*, **45**, 613–629, doi:[10.1175/JPO-D-13-0225.1](https://doi.org/10.1175/JPO-D-13-0225.1).
- Nagai, T., A. Tandon, E. Kunze, and A. Mahadevan, 2015: Spontaneous generation of near-inertial waves by the Kuroshio Front. *J. Phys. Oceanogr.*, **45**, 2381–2406, doi:[10.1175/JPO-D-14-0086.1](https://doi.org/10.1175/JPO-D-14-0086.1).
- Olson, D., O. Brown, and S. Emmerson, 1983: Gulf Stream frontal statistics from Florida Straits to Cape Hatteras derived from satellite and historical data. *J. Geophys. Res.*, **88**, 4569–4577, doi:[10.1029/JC088iC08p04569](https://doi.org/10.1029/JC088iC08p04569).
- Osgood, K., J. Bane Jr., and W. Dewar, 1987: Vertical velocities and dynamical balances in Gulf Stream meanders. *J. Geophys. Res.*, **92**, 13 029–13 040, doi:[10.1029/JC092iC12p13029](https://doi.org/10.1029/JC092iC12p13029).
- Ramachandran, S., A. Tandon, and A. Mahadevan, 2014: Enhancement in vertical fluxes at a front by mesoscale-submesoscale coupling. *J. Geophys. Res. Oceans*, **119**, 8495–8511, doi:[10.1002/2014JC01021](https://doi.org/10.1002/2014JC01021).
- Rayleigh, L., 1880: On the stability, or instability of certain fluid motions. *Proc. Roy. Soc. London*, **9**, 57–70.
- Risien, C. M., and D. B. Chelton, 2008: A global climatology of surface wind and wind stress fields from eight years of QuikSCAT scatterometer data. *J. Phys. Oceanogr.*, **38**, 2379–2413, doi:[10.1175/2008JPO3881.1](https://doi.org/10.1175/2008JPO3881.1).
- Savidge, D., and J. Bane Jr., 2004: Gulf Stream meander propagation past Cape Hatteras. *J. Phys. Oceanogr.*, **34**, 2073–2085, doi:[10.1175/1520-0485\(2004\)034<2073:GSMP>2.0.CO;2](https://doi.org/10.1175/1520-0485(2004)034<2073:GSMP>2.0.CO;2).
- Shakespeare, C., and J. Taylor, 2014: The spontaneous generation of inertia-gravity waves during frontogenesis forced by large strain: Theory. *J. Fluid Mech.*, **757**, 817–853, doi:[10.1017/jfm.2014.514](https://doi.org/10.1017/jfm.2014.514).
- Shchepetkin, A., and J. McWilliams, 2005: The Regional Oceanic Modeling System (ROMS): A split-explicit, free-surface, topography-following-coordinate ocean model. *Ocean Model.*, **9**, 347–404, doi:[10.1016/j.ocemod.2004.08.002](https://doi.org/10.1016/j.ocemod.2004.08.002).
- Silva, A. D., C. Young, and S. Levitus, 1994: Algorithms and Procedures. Vol. 1, *Atlas of Surface Marine Data 1994*, NOAA Atlas NESDIS 6, 74 pp.
- Thomas, L., and T. Joyce, 2010: Subduction on the northern and southern flanks of the Gulf Stream. *J. Phys. Oceanogr.*, **40**, 429–438, doi:[10.1175/2009JPO4187.1](https://doi.org/10.1175/2009JPO4187.1).
- von Arx, W. S., D. F. Bumpus, and W. S. Richardson, 1955: On the fine-structure of the Gulf Stream front. *Deep-Sea Res.*, **3**, 46–65, doi:[10.1016/0146-6313\(55\)90035-6](https://doi.org/10.1016/0146-6313(55)90035-6).
- Vukovich, F. M., and B. W. Crissman, 1980: Some aspects of Gulf Stream western boundary eddies from satellite and in situ data. *J. Phys. Oceanogr.*, **10**, 1792–1813, doi:[10.1175/1520-0485\(1980\)010<1792:SAOGSW>2.0.CO;2](https://doi.org/10.1175/1520-0485(1980)010<1792:SAOGSW>2.0.CO;2).
- , —, M. Bushnell, and W. King, 1979: Gulf Stream boundary eddies off the east coast of Florida. *J. Phys. Oceanogr.*, **9**, 1214–1223, doi:[10.1175/1520-0485\(1979\)009<1214:GSBEOT>2.0.CO;2](https://doi.org/10.1175/1520-0485(1979)009<1214:GSBEOT>2.0.CO;2).
- Wolfe, C., and C. Cenedese, 2006: Laboratory experiments on eddy generation by a buoyant coastal current flowing over variable bathymetry. *J. Phys. Oceanogr.*, **36**, 395–411, doi:[10.1175/JPO2857.1](https://doi.org/10.1175/JPO2857.1).
- Yoder, J., L. Atkinson, T. Lee, H. Kim, and C. McClain, 1981: Role of Gulf Stream frontal eddies in forming phytoplankton patches on the outer southeastern shelf. *Limnol. Oceanogr.*, **26**, 1103–1110, doi:[10.4319/lo.1981.26.6.1103](https://doi.org/10.4319/lo.1981.26.6.1103).
- , —, S. Bishop, J. Blanton, T. Lee, and L. Pietrafesa, 1985: Phytoplankton dynamics within Gulf Stream intrusions on the southeastern United States continental shelf during summer 1981. *Cont. Shelf Res.*, **4**, 611–635, doi:[10.1016/0278-4343\(85\)90033-0](https://doi.org/10.1016/0278-4343(85)90033-0).